Non-thermal X-ray emission from Anomalous X-ray Pulsars

den Hartog, P.R.

Chapter 6

Detailed high-energy characteristics of AXP 4U 0142+61 - Multi-year observations with INTEGRAL, RXTE, XMM-*Newton* and ASCA

P.R. den Hartog[1], *L. Kuiper*[1], *W. Hermsen*[1,2], *V.M. Kaspi*[3], *R. Dib*[3], *J. Knödlseder*[4], *F.P. Gavriil*[5]

[1] SRON Netherlands Institute for Space Research, Sorbonnelaan 2, 3584 CA Utrecht, The Netherlands
[2] Sterrenkundig Instituut Anton Pannekoek, University of Amsterdam, Kruislaan 403, 1098 SJ Amsterdam, The Netherlands
Physics Department, McGill University, 3600 University Street, Montreal, PQ H3A 2T8, Canada
[3] Centre d'Étude Spatiale des Rayonnement, CNRS/UPS, 31028 Toulouse Cedex 4, France
[4] NASA Goddard Space Flight Center, Astrophysics Science Division, Code 662, X-ray Astrophysics Laboratory, Greenbelt, MD 20771, USA

Received: January 12, 2008 / Accepted April 3, 2008

Astronomy & Astrophysics in press

Abstract

4U 0142+61 is one of the Anomalous X-ray Pulsars exhibiting hard X-ray emission above 10 keV discovered with INTEGRAL. In this paper we present detailed spectral and temporal characteristics both in the hard X-ray (>10 keV) and soft X-ray (<10 keV) domains, obtained using data from INTEGRAL, XMM-*Newton*, ASCA and RXTE. Accumulating data collected over four years with the imager IBIS-ISGRI aboard INTEGRAL , the time-averaged total spectrum shows a power-law like shape with photon index $\Gamma = 0.93 \pm 0.06$. 4U 0142+61 is detected up to 229 keV and the flux between 20 keV and 229 keV is $(15.01 \pm 0.82) \times 10^{-11}$ erg cm^{-2} s^{-1}, which exceeds the energy flux in the 2–10 keV band by a factor of $\sim$2.3. Using simultaneously collected data with the spectrometer SPI of INTEGRAL the combined total spectrum yields the first evidence for a spectral break above 100 keV: Assuming for the spectral shape above 20 keV a logparabolic function the peak energy of 4U 0142+61 is 228^{+65}_{-41} keV. There is no evidence for significant long-term time variability of the total emission from 4U 0142+61. Both the total flux and the spectral index are stable within the 17% level (1σ). Pulsed emission is measured with ISGRI up to 160 keV. The 20–160 keV profile shows a broad double-peaked pulse with a 6.2σ detection significance. The total pulsed spectrum can be described with a very hard power-law shape with a photon index $\Gamma = 0.40 \pm 0.15$ and a 20–150 keV flux of $(2.68 \pm 1.34) \times 10^{-11}$ erg cm^{-2} s^{-1}. To perform accurate phase-resolved spectroscopy over the total X-ray window, we produced pulse profiles in absolute phase for INTEGRAL-ISGRI, RXTE-PCA, XMM-*Newton*-PN and ASCA-GIS. The two known pulses in all soft X-ray profiles below 10 keV are located at the same phases. Three XMM-*Newton* observations in 2003–2004 show statistically identical profiles. However, we find a significant profile morphology change between an ASCA-GIS observation in 1999 following a possible glitch of 4U 0142+61. This change can be accounted to differences in relative strengths and spectral shapes (0.8–10 keV) of the two pulses. The principle peak in the INTEGRAL pulse profile above 20 keV is located at the same phase as one of the pulses detected below 10 keV. The second pulse detected with INTEGRAL is slightly shifted with respect to the second peak observed in the soft X-ray band. We performed consistent phase-resolved spectroscopy over the total high-energy band and identify at least three genuinely different pulse components with different spectra. The high level of consistency between the detailed results from the four missions is indicative for a remarkable stable geometry underlying the emission scenario. Finally, we discuss the derived detailed characteristics of the high-energy emission of 4U 0142+61 in relation to three models for the non-thermal hard X-ray emission.

6.1 Introduction

Anomalous X-ray Pulsars (AXPs) are a special subset of young isolated neutron stars with pulse periods in the range $\sim$2–12 s and with high period derivatives on the order of $10^{-10} - 10^{-12}$ s s^{-1}. Their (anomalous) X-ray luminosities ($L_X \sim 10^{33} - 10^{35}$ erg s^{-1} within 2–10 keV) are orders of magnitude too high to be explained by rotational energy released due

to spin down. Different origins of energy budgets proposed to explain the high luminosities were not consistent with all observational characteristics of AXPs (c.f. Woods & Thompson 2006; Kaspi 2007, for a review and latest developments). However, for Soft Gamma-ray Repeaters (SGRs), which are another subset of young isolated X-ray pulsars with similar periods, a toroidal magnetic field in the neutron-star core as energy reservoir was proposed by Duncan & Thompson (1992). Their magnetar model for SGRs can explain the anomalous X-ray luminosities of AXPs by the decay of an ultra-high magnetic field ($B \gtrsim 10^{15}$G). The magnetar model also explains numerous of other observable characteristics from AXPs like the large period derivatives and bursting behaviour. Most features of the magnetar model can be found in Duncan & Thompson (1992); Thompson & Duncan (1993, 1995, 1996); Thompson et al. (2002). Observational evidence collected over the last five years clearly showed that AXPs and SGRs have multiply similar characteristics and therefore are now believed to be subsets of magnetars (Woods & Thompson 2006).

In this paper we will present new results on AXP 4U 0142+61. This particular AXP has a spin period of $P = 8.69$ s and a period derivative of $\dot{P} = 0.20 \times 10^{-11}$ s s^{-1}. The inferred surface magnetic field strength is $B = 3.2 \times 10^{19} \sqrt{P\dot{P}}$ G = 1.3×10^{14} G. In the 2–10 keV band this is the brightest persistent AXP with a luminosity $L_X \sim 1 \times 10^{35}$ erg s^{-1} assuming a distance of 3.6 kpc (Durant & van Kerkwijk 2006a).

A remarkable discovery with the hard X-ray/soft gamma-ray telescope INTEGRAL (Winkler et al. 2003) is the existence of a hard spectral component in the spectra of AXPs at energies above 20 keV. In 2004 Molkov et al. (2004) reported hard X-ray emission ($>$20 keV) from the position of AXP 1E 1841-045 in the supernova remnant G27.4+0.0 (Kes 73). Kuiper et al. (2004a) showed unambiguously that the hard X-rays indeed originate from the AXP and not from the supernova remnant by detecting pulsations in the hard X-ray emission from this source using *Rossi X-ray Timing Explorer* (RXTE) PCA and HEXTE data.

For two other AXPs INTEGRAL detections have been reported. Revnivtsev et al. (2004a) and den Hartog et al. (2004a) detected 1RXS J170849-400910 (hereafter 1RXS J1708-40) and 4U 0142+61, respectively. Also for these and for a fourth AXP, 1E 2259+586, Kuiper et al. (2006) discovered pulsed hard X-ray emission using RXTE PCA and HEXTE data.

The INTEGRAL total-emission spectra available for 1E 1841-045, 1RXS J1708-40 and 4U 0142+61 are all power-law like and hard. The spectra of these three AXPs have photon indices[1] of 1.32 ± 0.11, 1.44 ± 0.45 and 1.05 ± 0.11, respectively (Kuiper et al. 2006). Furthermore, den Hartog et al. (2007) performed a multi-frequency campaign in which 4U 0142+61 was observed from radio to hard X-rays almost simultaneously. A dedicated INTEGRAL observation of 1 Ms was part of this campaign. This observation yielded a power-law like spectrum up to 229 keV with a photon index of 0.79 ± 0.10 with a luminosity of 2.6×10^{35}ergs^{-1}, which is roughly 2000 times the maximum luminosity possible by energy release due to spin down.

Interestingly, 4U 0142+61 exhibited some bursting activities which were discovered during the RXTE monitoring of this source. A first burst was found on April 6, 2006 (Kaspi et al. 2006).

[1] Defining the power law as $F = F_0 \times E^{-\Gamma}$ with F_0 the normalisation in units of ph cm^{-2} s^{-1} keV^{-1} and Γ the photon index

Soon thereafter, on June 25, four more bursts were detected (Dib et al. 2006). During these last events, the source seemed to be in an active state. Furthermore, Gavriil et al. (2007) discovered a very large X-ray burst on February 7, 2007. This burst was extraordinary as it showed characteristics similar to a SGR giant flare, only less energetic. It started with a bright and short spike with a peak flux of $\sim 2.5 \times 10^{-8}$ erg cm^{-2} s^{-1} (2–60 keV) and in the first part of the decaying tail single pulsations of the AXP were visible. The extended tail lasted up to half an hour. The fluence (T_{90}) of this burst was $\sim 14.5 \times 10^{-8}$ erg cm^{-2} s^{-1} (2–60 keV), which is 6–88 times higher than the previous five bursts from 4U 0142+61. Moreover, the spectrum shows significant spectral features (Gavriil et al. 2008a).

Theoretical attempts to find physical explanations for the hard X-ray emission have started, but so far none of the models can explain all of the published properties and for some aspects the data cannot discriminate between the proposed models. More detailed observational results are required to further constrain the geometries of the production sites as well as allowed production processes. In the discussion (see, Sect. 6.5) we summarise the different theoretical approaches, the promising progress, but also their shortcomings.

In this work detailed hard X-ray characteristics are presented using all available INTEGRAL data for 4U 0142+61 to date. These include total spectra (pulsed + DC emission) both time-averaged (whole mission) as well as in 5 shorter time stretches to look for possible long-term time variability. We also analysed two Target of Opportunity observations performed shortly after the above mentioned burst activities to look for variability of any kind. Furthermore, the time-averaged total-pulsed spectrum as well as time-averaged phase-resolved pulsed spectra are presented.

In order to study possible relations between the hard ($>$10 keV) and soft ($<$10 keV) X-ray bands we have (re)analysed archival XMM-*Newton*, RXTE-PCA and ASCA-GIS data applying parameters and selections consistent with the INTEGRAL analyses.

6.2 Observations and analysis

6.2.1 INTEGRAL

The hard X-ray/soft gamma-ray (3 keV – 8 MeV) mission *INTErnational Gamma-Ray Astrophysics Laboratory* INTEGRAL (Winkler et al. 2003), has been operational since October 2002. For this work both main instruments IBIS and SPI are used. IBIS, *Imager on Board the INTEGRAL Satellite* (Ubertini et al. 2003), is a coded-mask instrument with a low-energy detector called *INTEGRAL Soft Gamma-Ray Imager* (ISGRI; Lebrun et al. 2003) which is sensitive between $\sim$20 keV and $\sim$300 keV and has a wide field of view (FOV) of $29^\circ \times 29^\circ$ (full-width zero response). The angular resolution is about $12'$. The *Spectrometer for INTEGRAL* (SPI; Vedrenne et al. 2003) is also a coded-mask instrument which is sensitive between $\sim$20 keV and $\sim$8 MeV. The FOV is $35^\circ \times 35^\circ$ (full-width zero response). This instrument is optimised for spectroscopy and has a modest angular resolution of $\sim 2.^\circ 5$. SPI is of particular use in this work for its better sensitivity to IBIS above $\sim$200 keV.

Table 6.1: *Summary of the INTEGRAL observations of 4U 0142+61. The following information is given: the revolution intervals; the observations time spans both in MJD as in calendar dates; the number of Science Windows; exposure times ($t_{\rm exp}$); and the effective on-source exposure ($t_{\rm eff}$).*

Rev.	Time span			ScWs	$t_{\rm exp}\,(\rm ks)$	$t_{\rm eff}\,(\rm ks)$
142–468	52985 – 53960	Dec. 12, 2003	– Aug. 13, 2006	1617	4494.4	2365.3
142–189	52985 – 53125	Dec. 12, 2003	– Apr. 30, 2004	404	963.2	342.0
202–269	53165 – 53367	Jun. 9, 2004	– Dec. 28, 2004	410	976.5	501.6
331–336	53550 – 53568	Jun. 29, 2005	– Jul. 17, 2005	265	867.6	827.9
384–396	53710 – 53745	Dec. 6, 2005	– Jan. 10, 2006	435	1334.3	420.6
452–468	53912 – 53960	Jun. 26, 2006	– Aug. 13, 2006	103	353.8	273.2
454 ToO	53918 – 53920	Jul. 2, 2006	– Jul. 4, 2006	59	213.7	209.7
528 ToO	54139 – 54142	Feb. 8, 2007	– Feb. 11, 2007	54	198.6	195.5

In its default operation modes, INTEGRAL observes the sky in dither patterns (Jensen et al. 2003). Typical pointings (Science Windows, ScWs) have integration times of $\sim$1800–3600 s. Table 6.1 lists the total exposure time for the selected ScWs for which 4U 0142+61 was within an angle of 14.°5 from the pointing direction of IBIS, as well as the effective on-source exposure, which is reduced due to off-axis viewing angles. Due to the visibility windows of this part of the Galaxy for INTEGRAL operations, the observations of the prime targets form groups of consequentive orbital revolutions (Revs).

There are three dedicated observations on 4U 0142+61. The first one was performed mid 2005 and lasted for 1 Ms and two were shorter Target of Opportunity (ToO) observations which were triggered by the bursting activities detected with RXTE on June 25, 2006 and February 7, 2007.

The data were screened for Solar flares and erratic count-rates due to the passages through the Earth's radiation belts. After screening 1671 ScWs, resulting in 4.7 Ms total exposure time, were available for the analyses.

6.2.1.1 INTEGRAL spectra from spatial analysis

For spectral analysis the IBIS-ISGRI data of all 1671 ScWs are reduced using the Off-line Scientific Analysis (OSA) software package version 5.1 (see Goldwurm et al. 2003). For each ScW deconvolved sky images are created in 20 energy intervals using exponential binning between 20 keV and 300 keV. For every energy band time averaged count rates are determined by averaging the count rates, weighted by the variances, from all deconvolved maps at the position of 4U 0142+61, for each set of consecutive observations and the total data set. To convert the count rates to flux values we have used the procedure described by Kuiper et al.

(2006). The measured AXP count rates are normalized to the Crab count rates, determined from Crab observations performed during INTEGRAL Rev. 102. The AXP fluxes in Crab units are converted into photon fluxes using a curved power-law shape;

$$F_\gamma = 1.5703(14) \times (E_\gamma/0.06335)^{-2.097(2)-0.0082(16)\times\ln(E_\gamma/0.06335)} \quad (6.1)$$

(Eq. 2 in Kuiper et al. 2006), where F_γ is expressed in ph/(cm^2 s MeV) and E_γ in MeV. Finally the spectra are imported in XSPEC version 12.3 (Arnaud 1996), which is used for the spectral fitting. All errors quoted in this paper are 1σ errors, unless stated otherwise.

The spectral analysis of SPI data is based on all (screened) data up to Rev. 336. The data were binned in 9 energy bins covering the 20 keV – 1 MeV energy range. For each of the energy bins, source fluxes have then been extracted using a maximum likelihood fitting procedure that considers the instrumental response of the telescope (Knödlseder 2004). The measured flux is then normalized to the Crab spectrum that has been obtained by fitting the SPI data of revolutions 43–45. Multiplication with the above-mentioned curved power-law Crab model results then into photon fluxes.

6.2.1.2 INTEGRAL timing analysis

For the INTEGRAL timing analysis, we have followed the procedure described by Kuiper et al. (2006). We only considered ISGRI data for this purpose. Data up to Rev. 396 are used (see Table 6.1). Events are selected from non-noisy detector pixels that were/could be illuminated by the source through an open mask element with a greater illumination factor than 25%. Instrumental, on-board processing and ground-station time delays are corrected for (Walter et al. 2003). The event arrival times at the space craft are converted to arrival times at the Solar-system barycenter using the JPL DE200 Solar-system ephemeris and the source position measured with *Chandra* (Juett et al. 2002). The barycentered arrival times are finally folded on an appropriate phase-connected ephemeris (see Table 6.2) created using contemporaneous RXTE data (see Sect. 6.2.2). The (TDB) time to pulse phase conversion taking into account consistent phase alignment for each ephemeris is provided by the following formula:

$$\Phi(t) = \nu \cdot (t - t_{\rm Epoch}) + \frac{1}{2}\dot{\nu} \cdot (t - t_{\rm Epoch})^2 + \frac{1}{6}\ddot{\nu} \cdot (t - t_{\rm Epoch})^3 - \Phi_0. \quad (6.2)$$

The detection significances of the derived pulse profiles are estimated applying the $Z^2_{\rm n}$ test (Buccheri et al. 1983).

In order to derive the spectrum of the pulsed emission, first the number of excess counts in the obtained pulse profiles above flat background/DC levels have to be determined. For this purpose, the pulse profiles for the selected energy bands are fitted with truncated Fourier series using two harmonics. The minimum of this fit is defined as the DC level. The excess counts are counted above this level and converted into flux units applying the same procedure for the Crab pulsar and normalising to the known Crab-pulsar spectrum (Eq. 3 in Kuiper et al. 2006);

$$F_\gamma = 0.4693(21) \times (E_\gamma/0.04844)^{-1.955(7)-0.0710(78)\times\ln(E_\gamma/0.04844)}. \quad (6.3)$$

Table 6.2: *Phase-coherent ephemerides derived from RXTE-PCA monitoring data, valid for the analysed INTEGRAL observations.*

Start [MJD]	End [MJD]	INTEGRAL range (Revs)	$t_{\rm Epoch}$ [MJD, TDB]	ν [Hz]	$\dot{\nu} \times 10^{-13}$ $[\mathrm{Hz\,s^{-1}}]$	$\ddot{\nu} \times 10^{-22}$ $[\mathrm{Hz\,s^{-2}}]$	Φ_0
52549	53169	001–203	52726	0.1150945693297	-0.267038	0.220	0.9442
53251	53619	230–353	53420	0.1150929854501	-0.263899	0.307	0.8906
53562	53745	334–396	53650	0.1150924611500	-0.267430	-0.319	0.2817

Phase-resolved spectra are similarly created using only excess counts within selected phase intervals (see Sect. 6.3.3).

6.2.2 RXTE

The *Rossi X-ray Timing Explorer* (RXTE) has been operational since 1996. For this work we use data from the Proportional Counter Arrays (PCA) onboard RXTE (Jahoda et al. 1996), which is a non-imaging instrument sensitive in the 2–60 keV energy range. The FOV is approximately 1° (FWHM).

Regular monitoring observations of 4U 0142+61 with the RXTE-PCA (Gavriil & Kaspi 2002) are the basis of the timing results in this paper. These observations allow us to create accurate phase-connected timing solutions. We have generated three new phase-connected ephemerides with consistent pulse alignment to cover the whole INTEGRAL-time span. The details of the ephemerides can be found in Table 6.2. They are in agreement with the solution presented by Dib et al. (2007a), who also present a phase-coherent timing solution over the period 1996–2006.

We have used the same RXTE-PCA data as listed in Table 1 of Kuiper et al. (2006) which were taken between March 1996 and September 2003 before the INTEGRAL observations, to perform spectral timing analyses analogous to the procedures outlined by Kuiper et al. (2006). We note that in the folding process of PCA data the application of ephemeris entry one of Table 6.2 results in pulse profiles which are shifted 0.543 in phase with respect to the profiles shown in Kuiper et al. (2006) for 4U 0142+61.

Irrespective of the energy band, the pulse-profiles can be described sufficiently accurate by truncated Fourier series with 3 harmonics above constant background levels. The excess (pulsed) counts above the background levels are converted into flux units using properly PCU exposure weighted energy response matrices (see e.g. Sect. 3.2 of Kuiper et al. 2006).

We have extracted a time-averaged total-pulsed spectrum and phase-resolved spectra adopting the same phase intervals as selected for INTEGRAL (see Sect.6.3.3). To derive unabsorbed (soft) X-ray spectra a Galactic Hydrogen absorption column of $N_{\rm H} = 0.57 \times 10^{22}$ cm^{-2} has been used (as fixed value) as determined from spectral analyses of XMM-*Newton* observations (see Sect. 6.3.1.4).

6.2.3 XMM-Newton

XMM-*Newton* (Jansen et al. 2001) has been operational since 2000. Onboard are three CCD cameras for X-ray imaging, namely two EPIC (European Photon Imaging Camera) MOS cameras (Turner et al. 2001) and one EPIC-PN camera (Strüder et al. 2001). All cameras have a FOV of $\sim 30'$ and are sensitive in the energy range $\sim$0.3–12 keV.

We have (re)analysed the four publicly available data sets acquired by XMM-*Newton* between 2002 and 2004. The data set taken on February 13, 2002 (Obs Id 0112780301) did not contain usable data for this work. The summary of the remaining 3 data sets can be found in Table 6.3. We designate these observations A, B and C, respectively. In this work we present only the results using the PN. We have also analysed the data from both MOS instruments and used this for consistency checks. The PN was in small-window mode during observation A and in timing mode during observations B and C. In parallel studies Rea et al. (2007b) and Gonzalez et al. (2008) also analysed these XMM-*Newton* observations. Gonzalez et al. (2008) also included private XMM-*Newton* data taken in 2006 and 2007 together with *Chandra* and *Swift* data to study long-term variations below 10 keV.

The three data sets in Table 6.3 have been analysed using SAS v. 7.0 and the latest calibration files that were available (Jan. 2007). The data have been checked for solar (soft proton) flares by creating a light curve for each observation for events with energies larger than 10 keV. From these light curves the count-rate distribution has been determined and subsequently fitted with a Gaussian. Good Time Intervals (GTIs) have been created by allowing only time stamps from time intervals for which the count rate was lower than the fitted mean count rate plus three times the width of the distribution (3σ). For observations A, B and C these cutoff values were 0.082, 0.243 and 0.358 counts per second. PN single and double events, i.e. patterns less than and equal four, and an energy range of 0.3 to 12.0 keV have been selected. The arrival times of the selected events are barycentered adopting the most accurate celestial position of 4U 0142+61 (Juett et al. 2002).

There was no need to correct for pile up in observation A as the count rate from 4U 0142+61 was sufficiently low for the small-window mode. A circular extraction region centered at 4U 0142+61 with a radius of $40''$ was used. For the background extraction two circular source-

Table 6.3: *XMM-Newton observations of 4U 0142+61. The observations are designated A, B and C and referenced accordingly in the text. Further, the observation dates, exposures and Good Time Interval (GTI) exposures for MOS and PN are given.*

#	Obs ID	Date	Exp. (ks)	GTI-MOS (ks)	GTI-PN (ks)
A	0112781101	2003-01-24	6.4	5.4	3.7
B	0206670101	2004-03-01	46.5	36.4	27.3
C	0206670201	2004-07-25	23.9	23.0	20.6

free regions centered at different locations in the small-window were chosen with radii of 35″ and 47.″5, respectively.

Observations B and C were taken in timing mode. For these observations we chose extraction regions with a total width of 27 pixels centered on the source, which corresponds to 110.″7 close to the 95% encircled energy radius of the source. While the sensitive area (ARF) generator corrects for the remaining ∼5% of missed energy outside the source extraction region, it does not compensate for the subtraction of any source contribution in the chosen background extraction strip. We took a strip of 11 pixels wide starting 102.″5 from the point-spread function (PSF) core. The source contribution from this part of the PSF can be neglected. We fitted a Lorentzian plus constant background to the observed one-dimensional source profile. The source contribution in the 11 pixel wide background strip turned out to be a mere 0.48% of the normalized PSF, which means taking into account the source-to-background scaling of 27/11 an ignored correction of about 1.2%.

The extracted spectra have been binned, oversampling the energy resolution by a factor of three and then occasionally rebinned to ensure a minimum of 25 counts per bin.

For the XMM-*Newton* timing analysis, the events selected as described above are used. These events are folded using the appropriate ephemeris in Table 6.2. For the pulsed spectra the pulsed excess counts are extracted using the same procedure as described in Sect. 6.2.1.2 for the INTEGRAL pulsed spectrum, fitting the pulse profiles with truncated Fourier series with the first three harmonics above a constant background.

6.2.4 ASCA

ASCA (Tanaka et al. 1994) was operational for eight years from 1993. Onboard ASCA was the *Gas Imaging Spectrometer* (GIS, Ohashi et al. 1996; Makishima et al. 1996). The GIS was sensitive between ∼0.7–12 keV and had a FOV of ∼50′.

We have revisited the spectral timing analysis by Kuiper et al. (2006) of the ASCA-GIS observation of 4U 0142+61 taken in July/August 1999 to make it consistent with this work, i.e., in the current spectral analysis we have changed and fixed the Galactic absorption column to the value derived from the XMM-*Newton* data (see Sect. 6.3.1.4). In the timing analysis the pulse phase has been redefined to be consistent with that of INTEGRAL, RXTE and XMM-*Newton*, allowing the same phase selections for the phase-resolved spectroscopy.

6.3 Results

In this section, we will first present the INTEGRAL and XMM-*Newton* total spectra and the search for long-term variability. Next, we will present pulse profiles from our timing analyses of INTEGRAL, XMM-*Newton*, RXTE and ASCA. Finally, for the same instruments the total pulsed and phase-resolved spectra are derived consistently, revealing that genuinely different components contribute to the total pulsed emission.

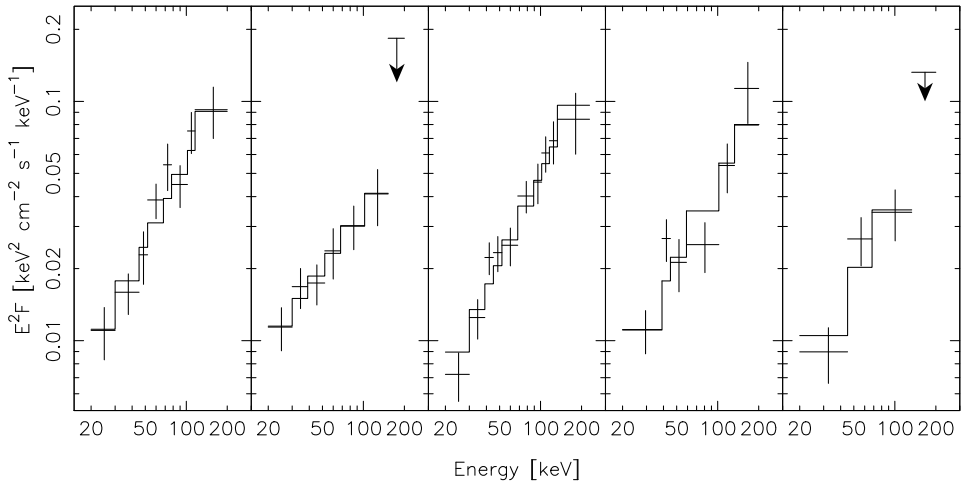

Figure 6.1: *Total-flux spectra of 4U0142+61 taken during INTEGRAL revolutions (from left to right); 142–189, 202–269, 331–336, 384–396 and 452–468. Data points are binned to* 4σ *if the single bins are of less significance. The upper limits represent* 2σ *confidence levels.*

6.3.1 Total spectrum and long-term variability

Previous INTEGRAL studies by den Hartog et al. (2006, 2007) and Kuiper et al. (2006) show that hard X-rays from 4U 0142+61 have been detected at different epochs at similar flux levels, suggesting a stable and persistent hard X-ray spectrum. Firstly, we will verify the stable nature of the high-energy emission. Then, we will present the time-averaged total spectrum using contemporaneous IBIS-ISGRI and SPI data. Finally, the total spectra of XMM-*Newton* are derived and an example is shown together with the INTEGRAL time-averaged total spectrum, rendering a broad-band X-ray view of the total spectrum.

6.3.1.1 INTEGRAL ISGRI persistent spectra and long-term variability

The ISGRI data were grouped in five sets as indicated in Table 6.1 and analysed as described in Sect. 6.2.1.1. The statistical quality is not equal for every spectrum, but 4U 0142+61 is detected significantly in each group and spectra can be extracted from each data set. The resulting five total spectra are displayed in Fig. 6.1.

To fit the spectra we use single power-law models. As in previous work they describe the spectral shapes at a satisfactory level. The fit results for these spectra are listed in the upper part of Table 6.4. The photon indices Γ range from 0.79 ± 0.10 to 1.21 ± 0.16 and the fluxes in the 20–150 keV energy band (F_{20-150}) range from 7.8×10^{-11} to 11.3×10^{-11} erg cm^{-2} s^{-1}.

The errors in the indices Γ and fluxes F_{20-150} are not independent. In order to check for possible long-term time variability we therefore compared the error contours of the different fits

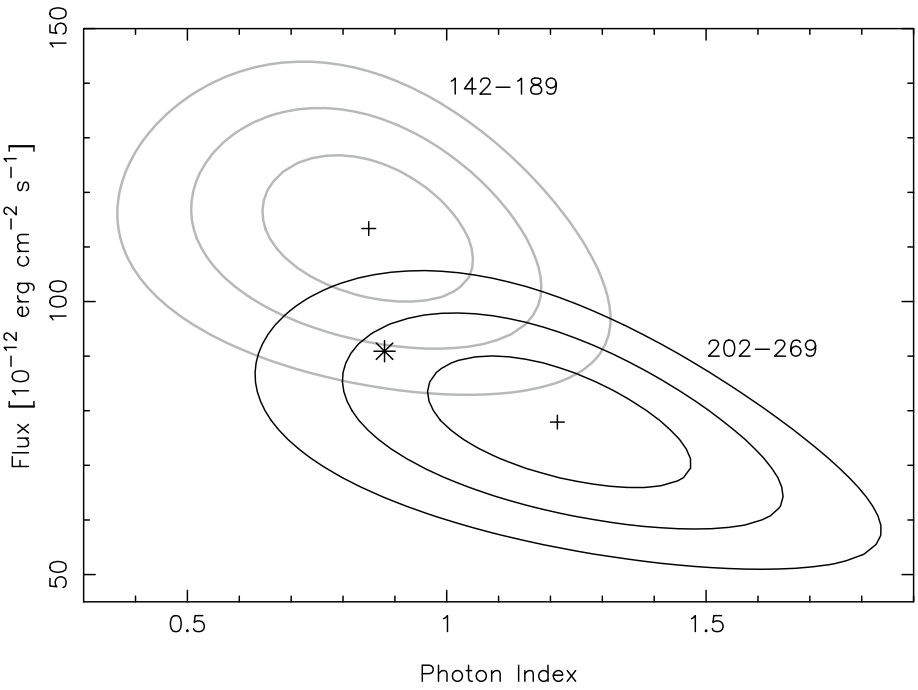

Figure 6.2: *Error contours ($1\sigma, 2\sigma$ and 3σ) of observations 142–189 (in grey) and 202–269 (in black) with respect to the time-averaged measurement (star).*

with respect to the error contours of the fit to the time-averaged total spectrum (see below in Sect. 6.3.1.2). The spectra extracted for Revs. 142–189 and 202–269 are the most deviating with respect to the time-averaged spectrum. In Fig. 6.2 the error contours for these spectra are shown together with the best-fit values for the time-averaged total spectrum (Revs. 142–468). The two spectra deviate from the average around the $\sim 2\sigma$ level.

The standard deviations ($s = \sqrt{1/(n-1)\sum_i (x_i - \bar{x})^2}$) for the power-law indices and the 20–150 keV fluxes relative to the weighted means are 0.16 and 1.5×10^{-11} erg cm^{-2} s^{-1}, respectively. Therefore, both the power-law shape and the 20–150 keV flux of 4U 0142+61 are stable within 17% (1σ).

6.3.1.2 INTEGRAL ISGRI & SPI total spectra

Using all available (Revs. 142–468, see Table 6.1) 2.37 Ms net on-source exposure the time-averaged total spectrum (Fig. 6.3) derived from ISGRI data can be fitted satisfactorily with a single power-law model. The best fit parameters give a photon index $\Gamma = 0.93 \pm 0.06$ and a 20–150 keV flux of $(9.09 \pm 0.35) \times 10^{-11}$ erg cm^{-2} s^{-1}. 4U 0142+61 has been detected up

Table 6.4: *Summary of the single power-law fits for the INTEGRAL-ISGRI total-spectra of 4U 0142+61 at different epochs for the observations summarized in Table 6.1. For each epoch the photon index, 20–150 keV flux and χ^2_r are given. For the the spectrum taken in Rev. 142–468 also the 20–229 keV flux is given.*

Rev.	Γ	$F_{20-150} \times 10^{-11}$ [erg cm^{-2} s^{-1}]	χ^2_r (dof)
142–189	0.85 ± 0.14	11.34 ± 0.78	0.69 (15)
202–269	1.21 ± 0.16	7.80 ± 0.83	0.66 (13)
331–336	0.79 ± 0.10	9.80 ± 0.57	1.12 (16)
384–396	0.89 ± 0.17	9.46 ± 0.91	0.91 (15)
452–468	0.96 ± 0.25	7.8 ± 1.2	0.82 (12)
454 ToO	1.06 ± 0.30	7.8 ± 1.4	0.98 (12)
528 ToO	0.88 ± 0.34	9.3 ± 1.8	1.63 (11)
142–468	0.93 ± 0.06	$9.09 \pm 0.35^{\dagger}$	0.94 (16)

$^{\dagger} F_{20-229} = (15.01 \pm 0.82) \times 10^{-11}$ erg cm^{-2} s^{-1}

to 229 keV with a 4.3σ significance in the 152–229 keV band.

Even though the upper limits at MeV energies obtained with the Compton telescope COMPTEL onboard CGRO (den Hartog et al. 2006, also shown in Fig. 6.3) strongly suggest that the spectrum has to break at a few hundred keV, the ISGRI spectrum shows no indication for a spectral break. The quality of the fit (χ^2_r = 0.94; dof = 16) assuming a single power-law model over the 20-300 keV range is good and the use of a more complex model with additional parameters is statistically not justified.

SPI is more sensitive than ISGRI at energies higher than ∼200 keV. Therefore, we have also analysed all available SPI data with 4U 0142+61 in the FOV. We have extracted the SPI spectrum and detected 4U 0142+61 significantly above 40 keV up to 140 keV. The maximum detection significance is 5σ between 80 keV and 140 keV. In the next energy bin (140–220 keV) a marginal detection of 2.6σ is achieved. The six flux values between 20 and 220 keV can be fitted (χ^2_r = 1.67; dof = 4) with a power-law model with photon index $\Gamma = 0.86 \pm 0.20$ and a 20–150 keV flux of $(8.8 \pm 1.2) \times 10^{-11}$ erg cm^{-2} s^{-1}, which is consistent with the ISGRI total spectrum (see Fig. 6.3).

Fitting the SPI spectrum with a single power law using all 9 spectral bins between 20 and 1000 keV we find a poor and unsatisfactory fit with a χ^2_r = 2.57 for 7 dof ($\chi^2 = 18$). Therefore, we followed Kuiper et al. (2006), by using a logparabolic function;

$$F = F_0 \times \left(\frac{E}{E_0}\right)^{-\alpha-\beta\cdot\ln\left(\frac{E}{E_0}\right)} \tag{6.4}$$

with E_0 (in units keV) the pivot energy introduced to minimize correlations between the param-

eters, and F_0 the flux (in units ph cm^{-2} s^{-1} keV^{-1}) at E_0. Note that this function is a simple power law if the curvature parameter β is equal to zero.

The fit of the SPI spectrum improves with $\Delta\chi^2_1 = 15.77$, which corresponds to a $\sim 4\sigma$ improvement for one additional fit parameter.

To exploit all available spectral information we fitted the ISGRI and SPI spectra simultaneously. Starting from a single power-law model we obtained a fit with a χ^2_r = 1.58 for 27 dof ($\chi^2 = 42.8$) which can be improved significantly. The model described by this power-law is too high in the energy range with the SPI upper limits i.e. above 220 keV. Using again a logparabolic function an optimum fit with a χ^2 of 20.1 is achieved. A $\Delta\chi^2_1$ of 22.7 for one additional parameter translates in a 4.8σ fit improvement. This is the *first* clear detection of the spectral break in the total spectrum of 4U 0142+61 above 20 keV using contemporaneous high-energy data. The best fit parameters are $\alpha = 1.26 \pm 0.09$, $\beta = 0.41 \pm 0.09$ and $F_0 = (5.1 \pm 0.3) \times 10^{-6}$ ph cm^{-2} s^{-1} keV^{-1} at E_0 = 91.527 keV. The peak energy (for a νF_ν representation, eq. to E^2F) corresponding to these parameters is $E_{\rm peak} = 228^{+106}_{-53}$ keV, while the 20–150 keV flux amounts: $(8.97 \pm 0.86) \times 10^{-11}$ erg cm^{-2} s^{-1} (fitting three free parameters).

Including the non-contemporaneous COMPTEL (0.75–30 MeV) flux measurements (upper limits in Fig. 6.3) in a similar fit yielded best fit parameters with somewhat smaller uncertainties. We found as best fit parameters: $\alpha = 1.484 \pm 0.057$, $\beta = 0.351 \pm 0.044$ and $F_0 = (3.01 \pm 0.16) \times 10^{-6}$ ph cm^{-2} s^{-1} keV^{-1} at E_0 = 133.718 keV. The peak energy (E^2F) corresponding to these parameters is $E_{\rm peak} = 279^{+65}_{-41}$ keV. We note that this result is based on an assumed "logparabolic" spectral shape. We adopted this spectral form in order to comply with the SPI and COMPTEL limits. However, we do not claim that we have measured the spectral shape above $\sim$200 keV in detail. In particular, the extension of the spectrum towards MeV energies is uncertain. Significant measurements in the energy range between 200 keV and 1 MeV are required to unravel the true spectral shape in the vicinity of the break energy.

6.3.1.3 INTEGRAL post-burst spectra

Of the five AXPs for which bursts have been detected, 4U 0142+61 is so far the only one for which a hard X-ray spectrum above $\sim$10 keV has been observed. After two remarkably different bursting events detected with RXTE-PCA we requested two INTEGRAL ToO observations in order to study possible correlations between the soft- and hard X-ray emission. For both occasions $\sim$200 ks ToO time was granted. The source was observed in Revs. 454 and 528 (see Table 6.1).

We have detected 4U 0142+61 with detection significances in the 20-150 keV energy band of 5.4σ and 5.9σ for Rev-454 and Rev-528, respectively. Both spectra have been fitted with a power-law model which described the spectra well. The fit parameters for the first ToO are $\Gamma = 1.06 \pm 0.30$ and $F_{20-150} = (7.8 \pm 1.4) \times 10^{-11}$ erg cm^{-2} s^{-1}and for the 2nd ToO the fit parameters are $\Gamma = 0.88 \pm 0.34$ and $F_{20-150} = (9.3 \pm 1.8) \times 10^{-11}$ erg cm^{-2} s^{-1}. The values

are fully consistent with those for the time-averaged spectrum[2] (see also Table 6.4).

Gonzalez et al. (2008) reported a flux increase of (15±3)% in the 2–10 keV band observed with XMM-*Newton* coinciding with the burst activity in 2006–2007. It should be noted, however, that in order to measure with INTEGRAL a significant ($>3\sigma$) change in the hard X-ray spectrum within a 200 ks observation, the flux level should have changed by at least $\sim$60%. Correlated changes in the hard and soft X-ray fluxes of the scale reported by Gonzalez et al. (2008) could therefore not be measured.

6.3.1.4 XMM-*Newton* EPIC-PN total emission spectra

We derived the XMM-*Newton* EPIC-PN total (= pulsed plus DC) spectra as described in Sect. 6.2.3 (see e.g. Fig 6.3 for an example). We first investigated the absorption column ($N_{\rm H}$) using the XMM observations with the best statistics (B and C) and concentrated ourselves on energies below $\sim$5 keV i.e. the soft part of the X-ray spectrum.

We used logparabolic functions in order for the spectra to bend downwards to the optical regime, as required by the broad-band spectrum (see e.g. the spectrum from the first broad-band campaign by den Hartog et al. 2007). If a traditional model, a combination of a black body and a power law, was chosen, the soft power-law component would keep increasing towards lower energies, which can only be compensated by increasing the absorption column. The latter would be forced to unrealistically high values (see e.g. Rea et al. 2007b, who derived $N_{\rm H} = (1.00 \pm 0.01) \times 10^{22}$ cm^{-2}). Fixing the $N_{\rm H}$ to the value published by Durant & van Kerkwijk (2006b, $N_{\rm H} = (0.64 \pm 0.07) \times 10^{22}$ cm^{-2}) from an accurate analysis of data of the Reflection Grating Spectrometer aboard XMM-*Newton* yielded, however, also poor fits at low energies between $\sim$0.6 keV and $\sim$1 keV in both observations B and C. Therefore, we treated $N_{\rm H}$ as a free parameter. For both observations we find an absorption column of $(0.57 \pm 0.02) \times 10^{22}$ cm^{-2}, which is somewhat lower than, but consistent with the value obtained by Durant & van Kerkwijk (2006b). Therefore, assuming that the origin of the absorption is Galactic and thus constant, we fix $N_{\rm H}$ to 0.57×10^{22} cm^{-2} for the rest of the XMM-*Newton* analyses. We note that Güver et al. (2008) find similar values for $N_{\rm H}$ by applying a surface thermal-emission and magnetosphere scattering model to the same XMM-*Newton* data in a parallel analysis.

Next, we consider the total XMM-*Newton* spectral energy window up to $\sim$12 keV. An additional model component is required to describe at least a part ($< 20\%$) of the harder ($\sim$5–12 keV) X-ray emission from both observations B and C. For this component a second logparabolic function is introduced, instead of the traditionally introduced power-law component. Furthermore, a third logparabolic component with *fixed* model parameters prescribed by the ISGRI/SPI joint fit above 20 keV (see Sect. 6.3.1.2) contributes in this energy band and is included in the total fit. Without the need to introduce an XMM-*Newton*-ISGRI inter-calibration

[2]Note that the 1st ToO is included in the time-averaged total spectrum, but we have tested the ToO with the time-averaged total spectrum of the first four data sets from which it was not statistically different.

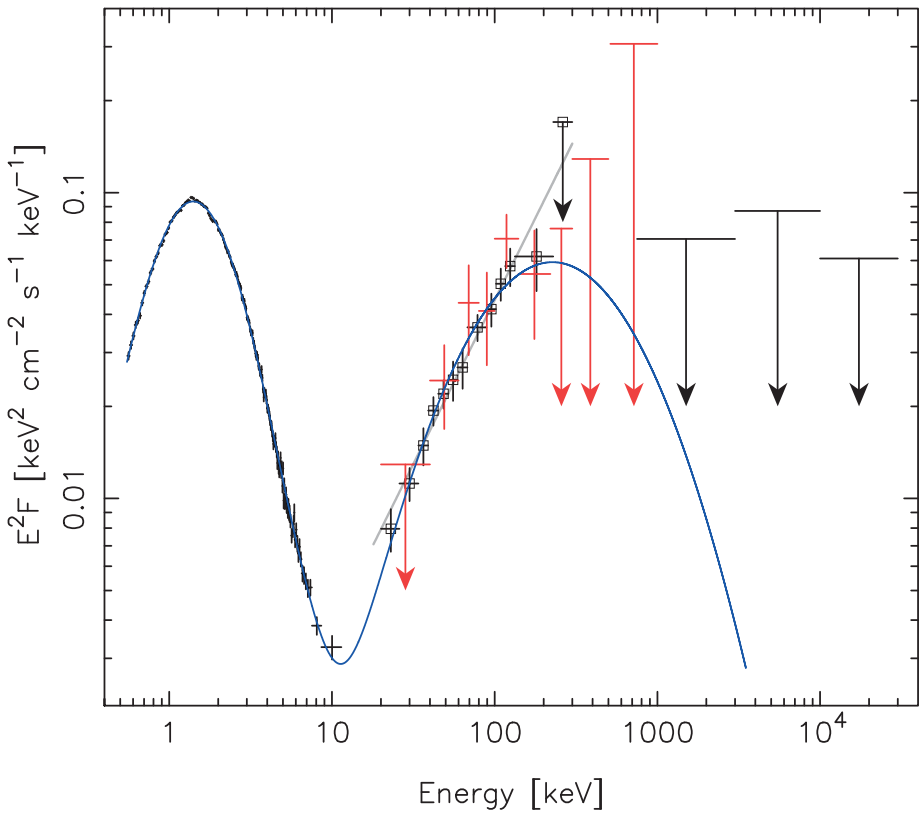

Figure 6.3: *Unabsorbed total spectra of 4U 0142+61 as measured with different instruments; XMM-Newton (Obs B; 0.55–11.5 keV) in black; INTEGRAL-ISGRI (Revs. 142–468; 20–300 keV) in black with open square symbols; INTEGRAL SPI (20–1000 keV) in red; and CGRO COMPTEL (0.75–30 MeV) limits in black. Shown are also the best single power-law model fit for the ISGRI data-points (in grey) and the 'three logparabola' fit for the whole band (in blue). See Sect. 6.3.1 for details.*

factor, a good fit was obtained to the high-energy parts of the XMM-*Newton* spectra. In Table 6.5 the fit results are presented for the three XMM-*Newton* observations.

However, for both long observations (obs. B and C) statistically unacceptable fits are obtained employing this empirical approach. Namely, significant residuals are apparent below 2 keV, because the logparabolae cannot follow the spectral shape exactly at these low energies. The small deviations from the optimum fit (hardly visible in Fig. 6.3) are of the order of a few percent for energies below 2 keV. We use the spectral fits, however, primarily for the conversion of absorbed fluxes into unabsorbed fluxes (data points shown in Fig. 6.3) by cal-

Table 6.5: *XMM-Newton EPIC-PN spectral fits of the total-emission spectrum of 4U 0142+61. Three logparabolae (Eq. 6.4) were used for an empirical fit including three fixed parameters from the ISGRI/SPI 20–1000 keV spectral fit. For each observation (A, B and C, see Table 6.3) six optimum parameter values are shown, three for each logparabolic model (indicated with a subscript number), for the best fit (0.55–10 keV). The last row lists the unabsorbed 2–10 keV energy flux in the units erg cm^{-2} s^{-1}.*

	A	B	C
$F_{0,1}$	$(6.85 \pm 0.05) \times 10^{-2}$	$(5.50 \pm 0.02) \times 10^{-2}$	$(4.57 \pm 0.02) \times 10^{-2}$
α_1	0.933 ± 0.012	0.673 ± 0.006	0.528 ± 0.008
β_1	1.534 ± 0.013	1.899 ± 0.007	2.089 ± 0.010
$F_{0,2}$	$(1.04 \pm 0.04) \times 10^{-2}$	$(2.33 \pm 0.02) \times 10^{-2}$	$(3.20 \pm 0.02) \times 10^{-2}$
α_2	2.095 ± 0.041	1.671 ± 0.009	1.440 ± 0.008
β_2	0.212 ± 0.025	0.622 ± 0.007	0.808 ± 0.006
$F_{2-10\,\mathrm{keV}}$	$(6.68 \pm 0.40) \times 10^{-11}$	$(6.27 \pm 0.14) \times 10^{-11}$	$(6.49 \pm 0.15) \times 10^{-11}$

a) The photon fluxes $F_{0,1}$ and $F_{0,2}$ are expressed in ph cm^{-2} s^{-1} keV^{-1}at E_0 = 1 keV.
b) Error estimates (1σ) in the fit parameters are obtained by fixing all parameters except the parameter of interest at their optimum values and subsequently determining, where the parameter of interest reaches a $\Delta\chi^2_{6-1}$ step of 7.038 from the global minimum. This increment corresponds to a 1σ step for $6-1$ degrees of freedom.

culating for each energy bin the fraction of energy which is absorbed. In Sect. 6.3.3 we use these high-statistics unabsorbed total flux measurements in even broader bins for deriving the pulsed fraction as a function of energy, and the uncertainty in that analysis is dictated by the errors in the fluxes from the phase resolved analysis. Therefore, the empirical two plus one (fixed) logparabolae fits assuming a constant absorption column of 0.57×10^{22} cm^{-2} are sufficiently accurate for our purposes.

Note from Table 6.5 that the total unabsorbed 2–10 keV energy flux is consistent with being constant during the time span of the three XMM-*Newton* observations. This is in agreement with Rea et al. (2007b) and Gonzalez et al. (2008), however, Gonzalez et al. (2008) report a flux increase of (15$\pm$3)% (2–10 keV) between the epochs of our XMM-*Newton* observations A, B and C and the epochs after the bursting activities started in 2006. The flux levels around 10 keV of the three XMM-*Newton* spectra are rather similar. Fig. 6.3, showing only the XMM-*Newton* obs. B spectrum, is therefore a good representation of the total high-energy ($>$0.5 keV) spectrum, particularly showing the abrupt transition from soft to hard X-rays.

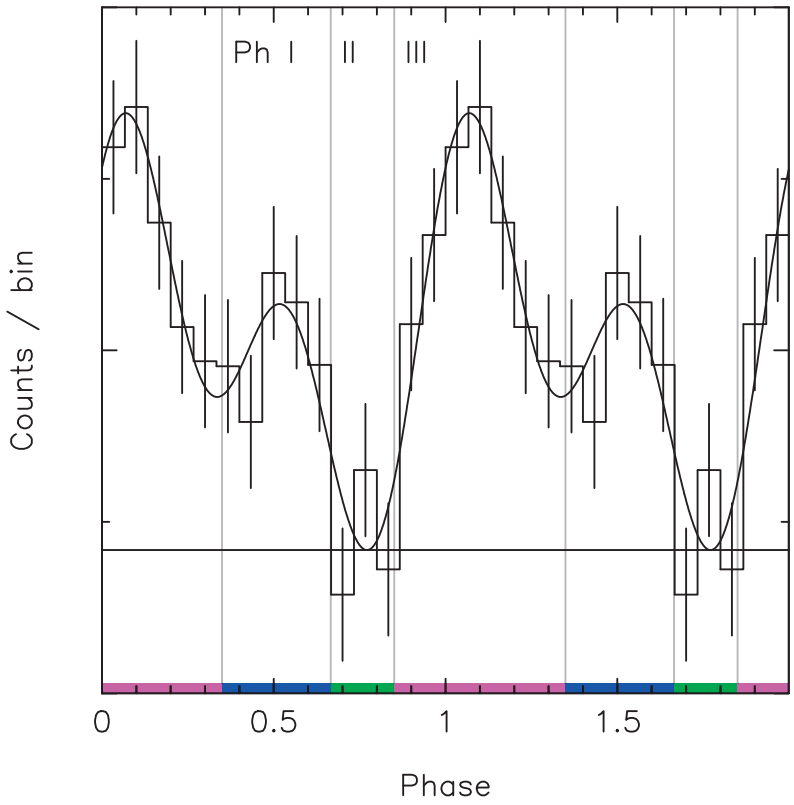

Figure 6.4: *20–160 keV ISGRI pulse profile of 4U 0142+61. The significance is* 6.5σ *using a* Z_2^2 *test (fit shown as solid curve). The fitted DC level is indicated with a horizontal line. Also indicated are the phase intervals for Ph I, II and III (see Table 6.6) with vertical grey lines and with colours.*

6.3.2 Timing analysis: pulse profiles

In this section we first present the time-averaged INTEGRAL IBIS-ISGRI pulse profiles of 4U 0142+61. Then, we will examine the XMM-*Newton* EPIC-PN and ASCA-GIS pulse profiles in single observations and test these for variability with time and energy, respectively. Finally, we compare the time-averaged ISGRI pulse profiles with the time-averaged XMM-*Newton* pulse profiles.

6.3.2.1 INTEGRAL ISGRI pulse profiles

Using the procedure described in Sect. 6.2.1.2 it is possible to detect significant pulsed emission from 4U 0142+61 in the ISGRI data. For the energy range 20–160 keV a maximum significance is reached of 6.5σ using a Z_2^2 test. The 20–160 keV pulse profile, shown in Fig. 6.4, is broad and appears to be double peaked with a DC level in a narrow phase interval of width $\sim$0.2.

Pulse profiles for the differential energy intervals 20–50 keV and 50–160 keV are shown in Fig. 6.7 E, F. The significances of the ISGRI pulse profiles are 4.4σ and 4.7σ, respectively, and are both more significant than the RXTE-HEXTE profiles for similar energy ranges (3.4σ and 2.0σ, respectively) shown in Kuiper et al. (2006). The profile for the 20–50 keV band (Fig. 6.7 E) shows the two peaks separated $\sim$0.5 in phase. The 50–160 keV profile (Fig. 6.7 F), however, shows only a shoulder to the first pulse at the location of the second pulse (near phase $\sim$0.5) in the 20–50 keV profile. The minimum (DC level) is in both cases located in the same narrow phase interval.

In order to quantify a possible pulse-morphology change as a function of energy, we performed a statistical method based on a combination of a Pearson χ^2 (see e.g. Sect. 11.2 of Eadie et al. 1971) and a Run test (see e.g. Sect. 11.3.1 of Eadie et al. 1971), comparing the shapes of the (independent) 20–50 keV and 50–160 keV pulse profiles. We did not apply the Kolmogorov-Smirnov test, because these background dominated (binned) ISGRI pulse phase distributions have different backgrounds and DC levels. In our approach we first obtained an appropriate model function describing the shape of the 20–50 keV pulse profile by fitting a truncated Fourier series using three harmonics. Next, we fitted the 50–160 keV distribution (in 20 bins) in terms of a constant and a function with free scale describing the shape of the 20–50 keV pulse profile (dof = 18). We investigated not only the absolute values of the deviation of the data from the optimum fit, but also the *signs* of the deviations by combining the probabilities from the independent Pearson χ^2 test (P_{χ^2}) and Run test (P_{run}) in an overall joint probability, $P = P_{\chi^2} \cdot P_{run}(1 - \ln P_{\chi^2} \cdot P_{run})$ (see e.g. Sect. 11.6 of Eadie et al. 1971). In our case the joint probability is 0.104, thus we cannot claim a significant difference in shape between the 20–50 keV and 50–160 keV ISGRI pulse profiles.

6.3.2.2 XMM-*Newton* and ASCA pulse profiles: time variability

The ASCA-GIS and RXTE-PCA pulse profiles published by Kuiper et al. (2006) suggested that the pulse profiles below $\sim$2–3 keV are significantly different. However, the RXTE-PCA pulse profiles were averages over years and the RXTE-PCA is not sensitive below 2 keV, contrary to ASCA-GIS . Dib et al. (2007a) used the 10 years of RXTE monitoring above 2 keV to show long-term variability in the pulse-profile shape. However, the reported effect is small; mainly the dip of emission between the two peaks got shallower between 2002 and 2006. Therefore, we used the ASCA-GIS and XMM-*Newton* observations to create pulse profiles in the same differential energy bands to test for time variability. The differences in the energy resolutions and responses between the two instruments has negligible impact on the comparison of the

profile shapes in the selected broad energy intervals.

Fig. 6.5 shows ASCA-GIS and XMM-*Newton* pulse profiles in the energy range 0.8–2.0 keV. This figure strongly suggests that the pulse profile taken with ASCA-GIS is different from the three XMM-*Newton* pulse profiles. For ASCA-GIS, the pulse that peaks around phase 0.6 is higher than the pulse that peaks around phase 1.1, while it is the other way around for all three XMM-*Newton* profiles. The latter profiles seem rather similar. We tested this applying the combination of the Pearson χ^2 and Run tests described in Sect. 6.3.2.1. The XMM-*Newton* profile with the highest statistics (Obs. B) was used as template. XMM-*Newton* profile A, with the lowest statistics, differs from profile B at the 1.8σ level, and profile C differs from profile B at the 2.6σ level. Slight differences in shapes are visible around the peaks of the two pulses, but we do not consider this evidence for significant time variability between the XMM-*Newton* observations. To the contrary, the ASCA-GIS profile for 0.8–2.0 keV differs from XMM-*Newton* profile B at the 16.6σ level. The above-mentioned differences in peak heights in the ASCA-GIS and XMM-*Newton* profiles become also clear when comparing the fluxes in these pulses (see Sect. 6.3.3.2 and Table 6.8). The pulse peaking at phase 0.6 contains $\sim$18% more flux than the average pulse during the XMM-*Newton* observations. The pulse peaking at phase 1.1 contains $\sim$34% less flux than the average pulse during the XMM-*Newton* observations.

Similar conclusions can be reached for the energy band above 2 keV for which the profiles are shown in Fig. 6.6. XMM-*Newton* profiles A and C differ from profile B at the 1.3σ and 3.5σ levels, respectively[3]; the ASCA-GIS profile for 2.0–8.0 keV deviates at the 9.3σ level. The variation is more drastic than the difference in profile shape may indicate. The flux in the GIS pulse peaking at phase 1.1 is 44% lower than the averaged flux in the same pulse in the XMM-*Newton* profiles. The flux in the GIS pulse peaking at phase 0.6 is only 12% reduced in flux. The difference is evident in Fig. 6.6 in which the profiles are approximately scaled to the measured 2–8 keV total pulsed flux.

We conclude that we found significant variability in the overall pulse-profile shapes for energies below 8 keV from the epoch of the ASCA observations (July/August 1999) to the epochs of the XMM-*Newton* observations in the years 2003–2004 (see Table 6.3). Particularly in the relative fluxes and spectra of the two pulses the change in shape is more drastic than reported before from RXTE-PCA observations by Dib et al. (2007a) and from more XMM-*Newton* observations by Gonzalez et al. (2008). Morii et al. (2005b) also report pulse-shape changes from the ASCA-GIS data. They use the 1999 observations (which we also use here) as a template to test two shorter observations from 1994 and 1998. Due to the low statistical quality of these data sets only significant changes below 3 keV could be claimed. Dib et al. (2007a) notice that the 1998 ASCA-GIS profile presented by Morii et al. (2005b) agrees with the pre-gap RXTE profile while the 1999 one does not. Interestingly, the profile measured with *Chandra* (Gonzalez et al. 2008) in May 2000 seems to be a transition between the ASCA-GIS (1999) and XMM-*Newton* profiles. If the deviant ASCA-GIS profile is caused by the glitch prior to this observation as proposed by Morii et al. (2005a), then it took about a year to get to the

[3] Rea et al. (2007b), analysing the same XMM-*Newton* observations obtained in 2004, also concluded that there are no significant differences in the profile shapes.

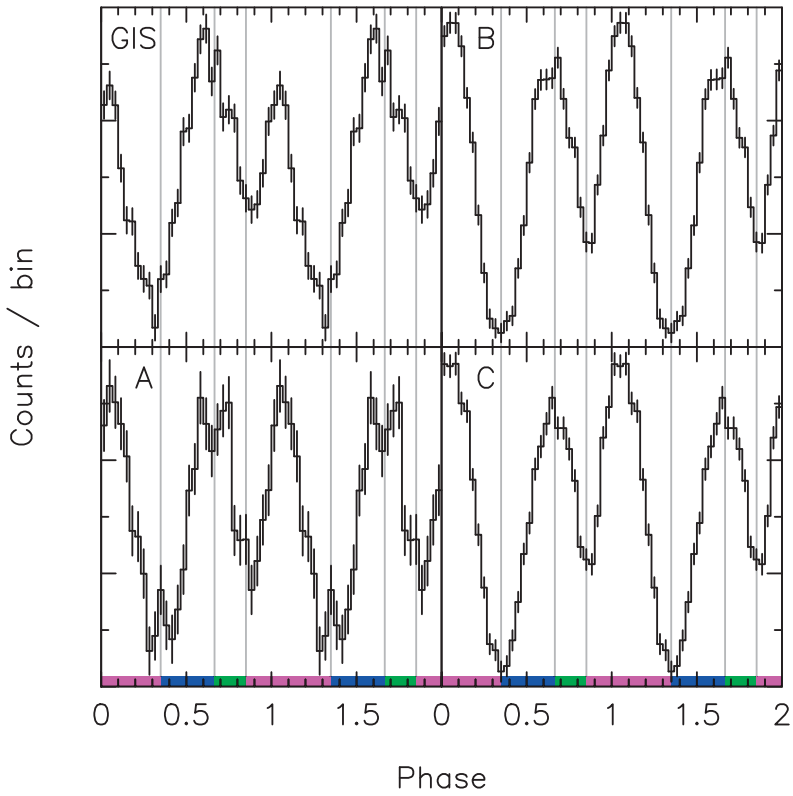

Figure 6.5: *4U 0142+61 pulse profiles for 0.8–2.0 keV of ASCA-GIS and the three XMM-Newton observations (A, B, C, Table 6.3). Phase intervals indicated as in Fig. 6.4. The profile of XMM-Newton observation C required a shift in phase by −0.028 for alignment with the profile of observation B (consistent with the other profiles). The relative normalization is consistent with the total pulsed flux (0.8–2.0 keV) being approximately constant (see Table 6.8).*

stable situation as measured with XMM-*Newton* in 2003–2004 and as can be seen from the RXTE pulse profiles (Dib et al. 2007a).

Apparently, some relatively fast reconfiguration in the pulse shape is ongoing during the 1999 ASCA-GIS and 2000 *Chandra* observations, which might be due to a proposed glitch (Morii et al. 2005b) or other drastic event.

6.3.2.3 Pulse-profile changes with energy

Kuiper et al. (2006) presented pulse profiles as a function of energy from ASCA-GIS, RXTE-PCA and HEXTE. From that work and e.g. Israel et al. (1999); Dib et al. (2007a); Rea et al.

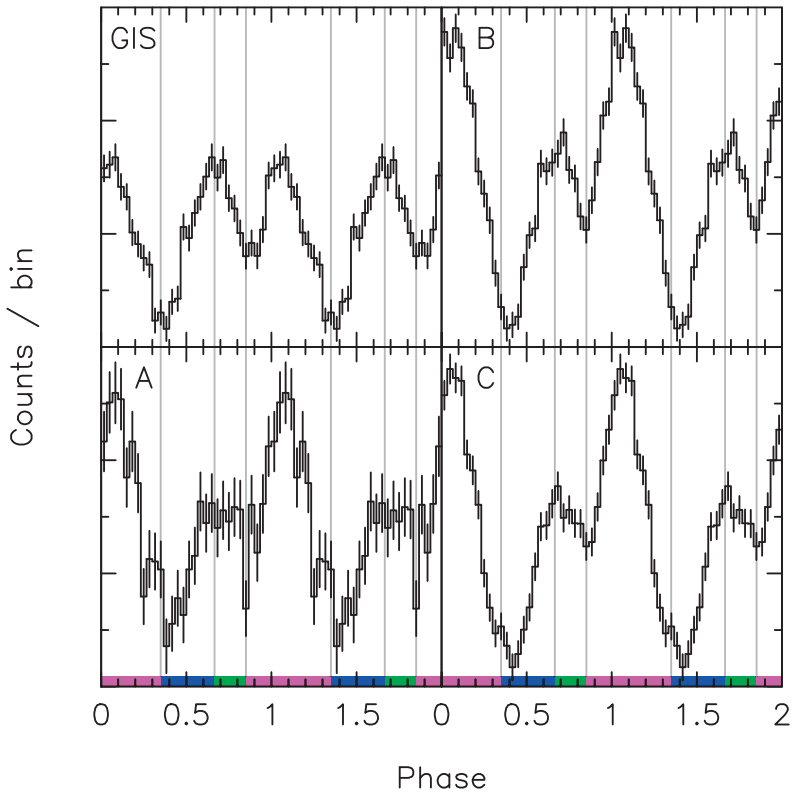

Figure 6.6: *4U 0142+61 pulse profiles for 2.0–8.0 keV of ASCA-GIS and the three XMM-Newton observations (A, B, C, Table 6.3). The relative normalization scales approximately with the total pulsed flux (2–8 keV; see e.g. Table 8). See also the caption of Fig. 6.5.*

(2007b) it is clear that the pulse profiles significantly change morphology with energy. In Sect. 6.3.2.2 we have shown that the pulse profiles of the 2003–2004 XMM-*Newton* observations are statistically the same. Therefore, we use in this section the summed 'time-averaged' pulse profile using all three XMM-*Newton* observations for comparison with maximal statistics with the profiles derived at higher energies with RXTE-PCA, and INTEGRAL.

In Fig. 6.7 time-averaged pulse profiles from XMM-*Newton*, RXTE-PCA, and ISGRI, are shown in 6 differential energy bands between 0.8 keV and 160 keV. It is evident that the morphology changes are ongoing throughout the energy range. One component that is apparent in all energy bands is the pulse that peaks around phase 1.1. Whereas the pulse that peaks at phase 0.7 in the XMM-*Newton* band is vanishing and no longer visible in the RXTE-PCA band, in the INTEGRAL band a pulse is visible around phase 0.5. In Sect. 6.3.3 we will disentangle

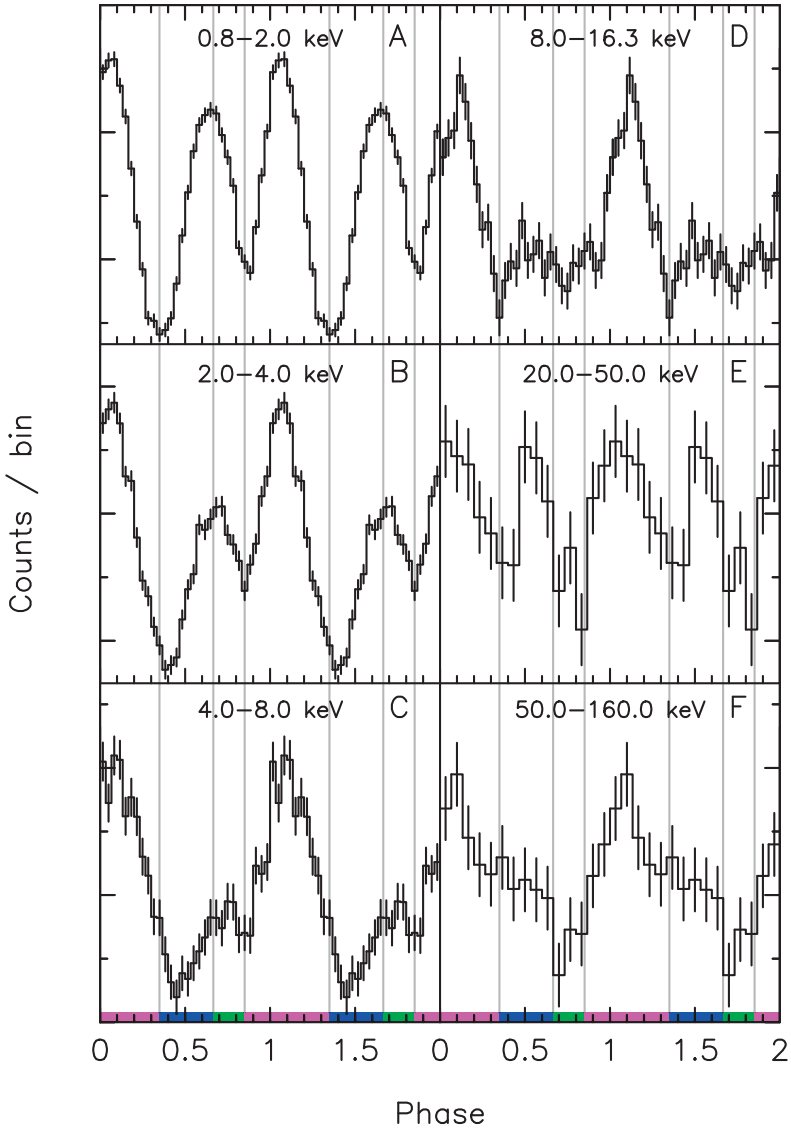

Figure 6.7: *4U 0142+61 pulse profiles from soft to hard X-rays. In panels A, B and C, pulse profiles in the energy ranges 0.8–2.0 keV, 2.0–4.0 keV and 4.0–8.0 keV are shown which are the sums of the XMM-Newton observations A, B, and C. Panel D presents the RXTE-PCA pulse profile in the energy band 8.0–16.3 keV taken from Kuiper et al. (2006). Finally, in panels E and F INTEGRAL pulse profiles are shown in the energy ranges 20–50 keV and 50–160 keV. Phase intervals are indicated as in Fig. 6.4.*

the contributions from different components using phase-resolved spectroscopy.

6.3.3 Timing analysis: total-pulsed and phase-resolved pulsed spectra

Total-pulsed spectra were created by the procedure described in Sect. 6.2.1.2. An example of how the excess counts in the pulsed components were extracted above a flat background level is shown in Fig. 6.4.

We performed phase-resolved spectroscopy for the first time for just the pulsed emission. Rea et al. (2007b) also performed phase-resolved spectroscopy with the XMM-*Newton* data. However, they did not separate the pulsed component from the dominant (on average $\sim$85%) DC component, which has a different spectrum and is invariant with phase. For our phase-resolved spectroscopy, we selected three phase intervals for which we want to extract high-energy spectra, using the morphology of the ISGRI 20–160 keV pulse profile (Fig. 6.4) for defining the phase boundaries: Ph I contains the smaller 2nd pulse in the INTEGRAL band, Ph II the DC level and Ph III contains the main pulse at hard X-rays, as well as the main pulse for energies below 10 keV. The definitions of the phase intervals are given in Table 6.6 and are indicated with grey vertical lines in all figures with pulse profiles.

Table 6.6: *Selected phase intervals for extraction of high-energy spectra, using the pulse-shape morphology of the INTEGRAL-IBIS-ISGRI 20–160 keV pulse profile (Fig. 6.4).*

	Phase interval	Component
Ph I	$[0.35, 0.666\rangle$	Secondary INTEGRAL pulse
Ph II	$[0.666, 0.851\rangle$	DC level INTEGRAL profile
Ph III	$[0.0, 0.35\rangle \vee [0.851, 1.0\rangle$	Main INTEGRAL pulse

6.3.3.1 INTEGRAL and RXTE

For the INTEGRAL data we constructed four broad-band pulse profiles in the energy ranges 20–40 keV; 40–80 keV; 80–160 keV and 160–300 keV. From these pulse profiles we got three total-pulsed flux measurements and one upper limit.

For RXTE-PCA, we extracted 14 pulse profiles in the energy band 2.5–31.5 keV for which we determined the number of excess counts (see Sect. 6.2.2). The last energy bin (23.8–31.5 keV) yielded no significant pulse profile, but the INTEGRAL and RXTE-PCA spectra nicely bridge the *minimum* luminosity.

The time-averaged total-pulsed spectra derived from INTEGRAL and RXTE-PCA data are presented in Fig. 6.8. The spectra are fitted simultaneously using a logparabola for the soft X-rays below 10 keV and either a power law or a logparabola for the hard X-rays. The fit results are summarized in Table 6.7. In Fig. 6.8 the fit with two logparabolae is plotted in black while the logparabola and a power-law fit is drawn in grey. Both fits to the INTEGRAL data are

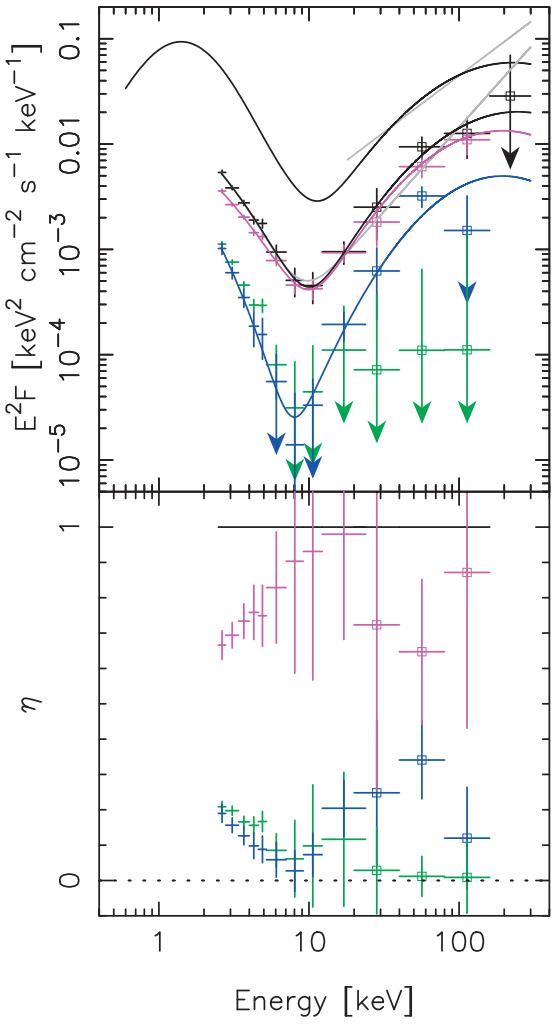

Figure 6.8: *In the top panel the phase-resolved pulsed-emission spectra and fits of INTEGRAL and RXTE-PCA are presented. The data points with a square symbol are INTEGRAL measurements and those without a marker are from RXTE-PCA. In black is presented the total-pulsed spectrum; in blue Ph I; in green Ph II; and in magenta Ph III. The arrows indicate the flux measurements with a significance less than 1.5σ. For comparison the INTEGRAL/XMM-Newton-B total-spectrum fit is drawn in black. Finally, in grey is plotted the power-law fit for the INTEGRAL total spectrum and the power-law fit for the total-pulsed spectrum. In the bottom panel η is presented in the same colour scheme as the spectra. η is defined as the fraction of the pulsed emission in a selected phase interval Ph I, Ph II or Ph III of the total-pulsed emission, i.e. the sum equals unity.*

Table 6.7: *RXTE-PCA and INTEGRAL spectral-fit parameters for the total-pulsed (TP) spectrum and for three phase intervals (see Table 6.6). The $N_{\rm H}$ is fixed to 0.57×10^{22} cm^{-2}. The subscripts below the fit parameters indicate if this parameter accounts for the soft (s, $<$10 keV) or hard (h, $>$10 keV) X-ray part of the spectrum. The normalizations ($F_{0\rm s}$ and $F_{0\rm h}$) are taken at E_0 = 1 keV and have the units ph cm^{-2} s^{-1} keV^{-1}.*

TP	Fit 1	Fit 2
$\alpha_{\rm s}$	2.27 ± 1.00	2.82 ± 1.08
$\beta_{\rm s}$	1.71 ± 0.90	1.10 ± 0.96
$F_{0\rm s}$	$(1.34 \pm 0.38) \times 10^{-2}$	$(1.79 \pm 1.23) \times 10^{-2}$
$\Gamma_{\rm h}$	0.40 ± 0.15	
$\alpha_{\rm h}$		-2.83 ± 2.16
$\beta_{\rm h}$		1.00 ± 0.67
$F_{0\rm h}$	$(9.17 \pm 4.47) \times 10^{-6}$	$(0.34 \pm 2.62) \times 10^{-8}$
χ^2_r (dof)	0.78 (13)	0.50 (12)
$F_{2-10\rm keV}$ (erg cm^{-2} s^{-1})	$(6.82 \pm 1.77) \times 10^{-12}$	$(6.85 \pm 0.93) \times 10^{-12}$
$F_{20-150\rm keV}$	$(2.68 \pm 1.34) \times 10^{-11}$	$(2.77 \pm 0.68) \times 10^{-11}$
Ph I		
$\alpha_{\rm s}$	2.90 ± 2.14	2.89 ± 3.66
$\beta_{\rm s}$	2.56 ± 2.88	2.42 ± 3.35
$F_{0\rm s}$	$(0.67 \pm 1.71) \times 10^{-2}$	$(0.63 \pm 1.74) \times 10^{-2}$
$\Gamma_{\rm h}$	0.12 ± 0.20	
$\alpha_{\rm h}$		-4.00 ± 4.62
$\beta_{\rm h}$		1.31 ± 0.72
$F_{0\rm h}$	$(5.78 \pm 8.81) \times 10^{-7}$	$(0.67 \pm 5.47) \times 10^{-9}$
χ^2_r (dof)	1.43 (13)	0.69 (12)
$F_{2-10\rm keV}$ (erg cm^{-2} s^{-1})	$(1.62 \pm 0.60) \times 10^{-12}$	$(1.14 \pm 3.64) \times 10^{-12}$
$F_{20-150\rm keV}$	$(5.99 \pm 3.29) \times 10^{-12}$	$(6.89 \pm 6.42) \times 10^{-11}$
Ph II		
$\alpha_{\rm s}$	2.95 ± 1.71	
$\beta_{\rm s}$	1.59 ± 1.56	
$F_{0\rm s}$	$(5.25 \pm 0.72) \times 10^{-3}$	
χ^2_r (dof)	0.86 (15)	
$F_{2-10\rm keV}$ (erg cm^{-2} s^{-1})	$(1.30 \pm 0.03) \times 10^{-12}$	
Ph III		
$\alpha_{\rm s}$	1.63 ± 0.59	2.68 ± 0.79
$\beta_{\rm s}$	2.07 ± 0.44	1.01 ± 0.70
$F_{0\rm s}$	$(5.55 \pm 2.34) \times 10^{-3}$	$(1.02 \pm 0.52) \times 10^{-2}$
$\Gamma_{\rm h}$	0.50 ± 0.11	
$\alpha_{\rm h}$		-2.99 ± 1.73
$\beta_{\rm h}$		1.09 ± 0.54
$F_{0\rm h}$	$(1.11 \pm 0.39) \times 10^{-5}$	$(0.26 \pm 1.67) \times 10^{-7}$
χ^2_r (dof)	1.1 (13)	0.65 (12)
$F_{2-10\rm keV}$ (erg cm^{-2} s^{-1})	$(4.72 \pm 0.52) \times 10^{-12}$	$(4.82 \pm 0.47) \times 10^{-12}$
$F_{20-150\rm keV}$	$(2.06 \pm 0.82) \times 10^{-11}$	$(2.07 \pm 1.09) \times 10^{-11}$

fully acceptable, but the single power-law model uses less parameters. It can be seen that if the hard X-ray spectrum has a power-law shape with $\Gamma = 0.4$ that the pulsed fraction could become as high as 100% around $\sim$250 keV. If the spectral shape is logparabolic, the pulsed fraction would not increase and it would stabilise around $\sim$30%–40%

For the three differential phase intervals (see Table 6.6) also spectra are extracted and plotted in Fig. 6.8. Immediately clear is that Ph III contains the bulk of the energy of the pulsed emission. The spectrum shows a similar transition (from soft to hard) as the total-pulsed spectrum. Also visible is that the soft X-ray spectrum ($<$10 keV) of Ph III is quite a bit harder than the soft X-ray spectra of Ph I and Ph II. While below 10 keV Ph I and Ph II form one pulse, in the INTEGRAL band only in Ph I is a pulse visible. From the spectrum and fit in Fig. 6.8 it can be seen that this transition for Ph I is extremely drastic from the very soft to the very hard.

We can not present an accurate pulsed fraction using RXTE-PCA data. *The pulsed fraction is defined as the pulsed flux (determined as described in Sect. 6.2) divided by the total flux from the point source (pulsed + DC).* The RXTE-PCA is a non-imaging instrument, making it difficult to determine a reliable total flux and spectrum due to confusion with RX J0146.9+6121, a closeby high-mass X-ray binary (Motch et al. 1991), and underlying Galactic-ridge emission (Valinia & Marshall 1998). Alternatively, we present η in the bottom panel of Fig. 6.8. η *is defined as the fraction of the pulsed emission in a selected phase interval of the total-pulsed emission.* From the η of Ph III (magenta) it can be seen that the contribution of this phase interval to the total-pulsed emission increases from $\sim$65% around 3 keV to practically 100% around 10 keV. The contributions of Ph I and Ph II gradually decrease from $\sim$20% at 2 keV to (consistent with) no contribution at 10 keV. The contribution of Ph II remains consistent with 0% in the INTEGRAL band (DC level), but the contribution to the pulsed emission from Ph I increases again as a result of the small 2nd peak in the INTEGRAL band. Because the pulsed contributions in both phase intervals Ph I and Ph II similarly decrease to $\sim$0% at 10 keV, and the pulse shape in the soft X-ray band seems to be of one component, we infer that the small 2nd pulse in the INTEGRAL band is unrelated to the soft X-ray pulse. It likely originates from a different site (height) in the magnetosphere but appears around the same phase as the soft X-ray pulse.

It is important to remember that the time-averaged RXTE-PCA spectra are assembled between March 1996 and September 2003, while the INTEGRAL observations are taken from December 2003 to August 2007. It is then remarkable how well the spectra (total pulsed and Ph III) connect in Fig. 6.8, suggesting stable emission (geometry) above $\sim$10 keV over 11 years.

6.3.3.2 XMM-*Newton* and ASCA

For the three XMM-*Newton* and ASCA observations we also determined the total-pulsed spectra as well as the pulsed emission spectra for the three selected phase intervals. Systematic uncertainties in the response for the timing mode of XMM-*Newton* above $\sim$8 keV prevented us from using the higher-energy data. For this reason the observational gap between XMM-*Newton* and INTEGRAL is about 12 keV.

In the top panels of Fig. 6.9 the results of ASCA-GIS and XMM-*Newton* obs. A, B and C are presented together with the INTEGRAL results of Fig. 6.8. The colour scheme is the same as in Fig. 6.8. In black are drawn the total-pulsed spectra and (except for ASCA-GIS) the (binned) total spectra. To the total spectra of XMM-*Newton* and INTEGRAL the best fits are drawn. In the panel for ASCA-GIS the fit to the total spectrum for XMM-*Newton* obs. C and INTEGRAL is drawn.

We have fitted each spectrum with a single logparabolic function. These fit results are given in Table 6.8. The parameters of a logparabolic function are not easy to compare, but the flux values indicate that there are some differences between the different observations, consistent with our findings in the comparison of the pulse shapes.

Most remarkable are flux differences between the ASCA-GIS observation and the XMM-*Newton* ones. (The latter are consistent with the fluxes reported by Gonzalez et al. 2008). While the 0.8–2 keV total-pulsed fluxes of all observations are comparable, the 2–10 keV total-pulsed flux of ASCA-GIS is significantly lower than the rest. From the phase-resolved spectra it becomes clear that this difference is due to the significantly lower flux (2–10 keV) in the main pulse (Ph III). In this phase interval the ASCA-GIS 2–10 keV flux is less than in the XMM-*Newton* observations, while the 2–10 keV flux for phases Ph I and Ph II are slightly lower than, or comparable to those measured with XMM-*Newton*. We note that the 0.8–2 keV ASCA-GIS flux in Ph III is somewhat lower than in the other observations. Note also that only for ASCA-GIS the 0.8–2 keV flux in Ph I is higher than, or comparable to, this flux in Ph III.

Table 6.8 shows that over the three XMM-*Newton* observations the total-pulsed flux in the 0.8–2 keV and 2–8 keV bands as well as the fluxes in all three phase intervals are statistically stable. The latter is consistent with the conclusion that the shape of the pulse profiles did not change measurably in this time interval.

6.3.3.3 Comparison

To determine the pulsed fraction as a function of energy we have binned the total spectra in the same binning as the total-pulsed and phase-resolved pulsed spectra. The pulsed fraction is defined as the pulsed flux (determined as described in Sect. 6.2) divided by the total flux from the point source (pulsed + DC). For the instruments ASCA-GIS and RXTE-PCA we do not have accurate total spectra, therefore we also consider η.

We start with the pulsed fraction. In the previous sections we showed that XMM-*Newton* observations A, B and C exhibit statistically identical pulse shapes and pulsed fluxes. Therefore, we have combined these observations by taking weighted averages. In Fig. 6.10 the pulsed fraction as a function of energy is presented for the averaged XMM-*Newton* and INTEGRAL observations (black data points). Also presented in this figure are the pulsed fractions for the three selected phase intervals (coloured data points). It can be seen in this figure that the pulsed fraction in the XMM-*Newton* band increases from $\sim$10% around 1 keV to $\sim$20% around 8 keV. This trend continues in the INTEGRAL band where the pulsed fraction is increasing to possibly as high as $\sim$40% in the 40–80 keV band. Rea et al. (2007b) presented the pulsed fraction of the fundamental and first harmonic sine functions for the XMM-*Newton*

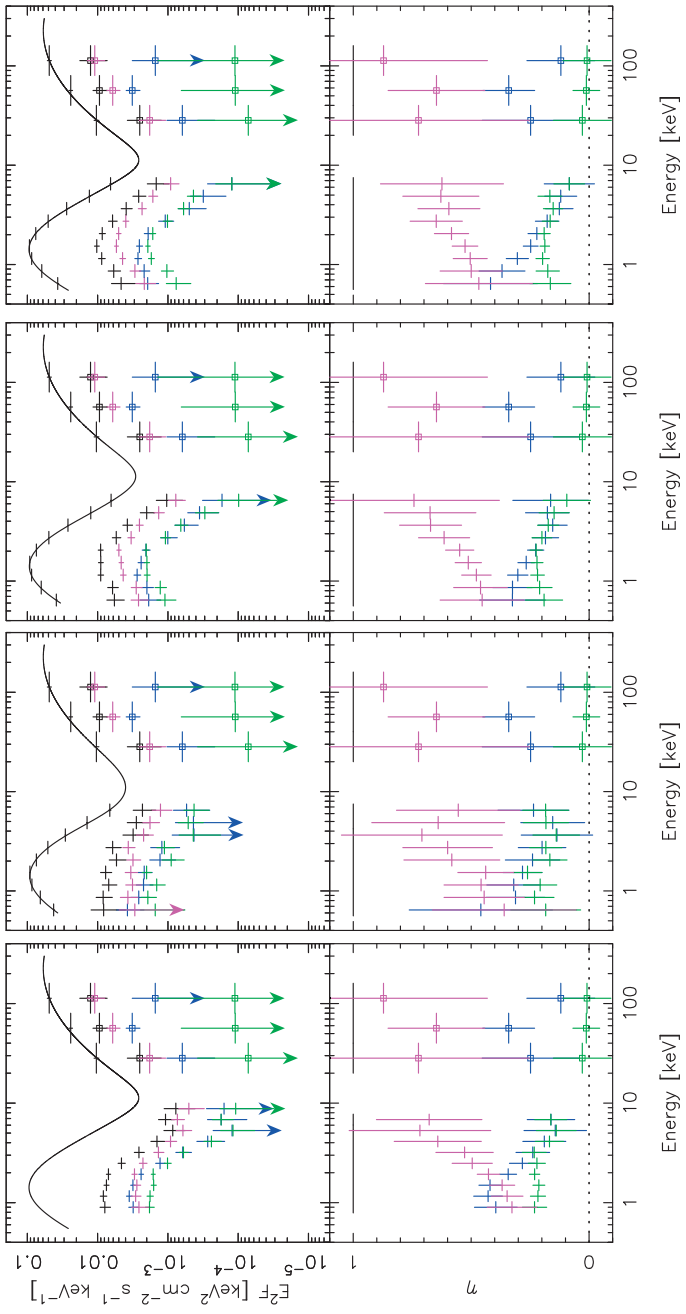

Figure 6.9: *For 4 (soft) X-ray and INTEGRAL observations we present the total, total-pulsed and phase-resolved pulsed spectra (top panels) and η (bottom panels, defined as the fraction of the total pulsed emission). The (soft) X-ray data from left to right are ASCA GIS, XMM-Newton PN obs. A, B and C. All data are equally binned for easy comparisons. For the total spectra, the best fit is shown. In the top panel for ASCA-GIS the best fit to the total spectrum of XMM-Newton obs. B and INTEGRAL are shown for clarity. The total spectra and total-pulsed spectra are plotted in black. The phase resolved spectra for Ph I, Ph II and Ph III (see Table 6.6) are plotted in blue, green and magenta, respectively. The INTEGRAL phase-resolved spectra are indicated in each figure with a square symbol. The data points with arrows indicate that the flux values have significances less than 1.5σ. The positive 1σ error is drawn. In the bottom panels η is presented in the same colour scheme as the spectra.*

Table 6.8: *ASCA-GIS and XMM-Newton (A, B & C) fits for the total-pulsed (TP) spectra and for spectra of three phase intervals (Ph I, II and III, see Table 6.6) for 4U 0142+61. The $N_{\rm H}$ is fixed to 0.57×10^{22} cm^{-2}. For each observation the three parameters of the parabola are given. The normalizations (F_0) are taken at E_0 = 1 keV and have the units ph cm^{-2} s^{-1} keV^{-1}. The integrated fluxes have the units erg cm^{-2} s^{-1}*

TP	ASCA-GIS	A	B	C
α	1.88 ± 0.30	2.19 ± 0.38	1.24 ± 0.15	1.12 ± 0.17
β	2.03 ± 0.48	0.65 ± 0.55	2.43 ± 0.26	2.41 ± 0.27
F_0	$(8.49 \pm 0.77) \times 10^{-3}$	$(7.93 \pm 0.10) \times 10^{-3}$	$(8.17 \pm 0.41) \times 10^{-3}$	$(7.98 \pm 0.45) \times 10^{-3}$
χ^2_r (dof)	1.8 (7)	0.29 (6)	0.88 (15)	0.86 (15)
$F_{0.8-2\,\rm keV}$	$(11.47 \pm 0.70) \times 10^{-12}$	$(10.96 \pm 1.38) \times 10^{-12}$	$(12.64 \pm 0.50) \times 10^{-12}$	$(12.72 \pm 0.56) \times 10^{-12}$
$F_{2-10\,\rm keV}$	$(5.55 \pm 0.33) \times 10^{-12}$	$(9.02 \pm 1.20) \times 10^{-12}$	$(8.16 \pm 0.35) \times 10^{-12}$	$(9.17 \pm 0.39) \times 10^{-12}$
Ph I				
α	1.54 ± 0.27	2.72 ± 0.47	1.57 ± 0.20	1.59 ± 0.20
β	3.76 ± 0.68	0.39 ± 0.84	2.71 ± 0.45	2.79 ± 0.45
F_0	$(3.49 \pm 0.28) \times 10^{-3}$	$(2.57 \pm 0.38) \times 10^{-3}$	$(2.53 \pm 0.14) \times 10^{-3}$	$(2.57 \pm 0.14) \times 10^{-3}$
χ^2_r (dof)	0.66 (7)	0.30 (6)	0.61 (15)	0.50 (15)
$F_{0.8-2\,\rm keV}$	$(4.58 \pm 0.46) \times 10^{-12}$	$(3.29 \pm 0.80) \times 10^{-12}$	$(3.56 \pm 0.27) \times 10^{-12}$	$(3.37 \pm 0.25) \times 10^{-12}$
$F_{2-10\,\rm keV}$	$(1.39 \pm 0.14) \times 10^{-12}$	$(1.83 \pm 0.52) \times 10^{-12}$	$(1.50 \pm 0.16) \times 10^{-12}$	$(1.36 \pm 0.12) \times 10^{-12}$
Ph II				
α	1.51 ± 0.31	2.24 ± 0.39	0.94 ± 0.18	0.97 ± 0.17
β	2.81 ± 0.52	0.83 ± 0.63	3.27 ± 0.34	2.97 ± 0.31
F_0	$(1.79 \pm 0.16) \times 10^{-3}$	$(1.80 \pm 0.23) \times 10^{-3}$	$(1.75 \pm 0.10) \times 10^{-3}$	$(1.51 \pm 0.08) \times 10^{-3}$
χ^2_r (dof)	1.73 (7)	1.09 (6)	0.96 (15)	1.35 (15)
$F_{0.8-2\,\rm keV}$	$(2.50 \pm 0.26) \times 10^{-12}$	$(2.44 \pm 0.50) \times 10^{-12}$	$(2.77 \pm 0.20) \times 10^{-12}$	$(2.41 \pm 0.18) \times 10^{-12}$
$F_{2-10\,\rm keV}$	$(1.13 \pm 0.10) \times 10^{-12}$	$(1.65 \pm 0.39) \times 10^{-12}$	$(1.51 \pm 0.10) \times 10^{-12}$	$(1.38 \pm 0.10) \times 10^{-12}$
Ph III				
α	1.87 ± 0.33	1.74 ± 0.43	1.05 ± 0.14	0.95 ± 0.14
β	1.36 ± 0.44	0.95 ± 0.55	2.31 ± 0.21	2.41 ± 0.20
F_0	$(3.03 \pm 0.37) \times 10^{-3}$	$(3.42 \pm 0.55) \times 10^{-3}$	$(3.86 \pm 0.19) \times 10^{-3}$	$(3.98 \pm 0.19) \times 10^{-3}$
χ^2_r (dof)	1.72 (7)	0.27 (6)	1.01 (15)	1.54 (15)
$F_{0.8-2\,\rm keV}$	$(4.23 \pm 0.58) \times 10^{-12}$	$(5.09 \pm 1.17) \times 10^{-12}$	$(6.30 \pm 0.37) \times 10^{-12}$	$(6.65 \pm 0.36) \times 10^{-12}$
$F_{2-10\,\rm keV}$	$(3.01 \pm 0.28) \times 10^{-12}$	$(5.37 \pm 0.82) \times 10^{-12}$	$(5.13 \pm 0.24) \times 10^{-12}$	$(5.63 \pm 0.22) \times 10^{-12}$

pulse profiles as a function of energy below 10 keV. These are consistent with the total pulsed fractions we show in Fig. 6.10.

Fig. 6.10 also shows that the trend set by the total-pulsed fraction is followed closely by the pulsed fraction that can be assigned to Ph III (magenta), as we have already discussed in Sect. 6.3.3.1. Ph III alone accounts for ∼5%–12% of the pulsed fraction between 1–8 keV. The other two phases do not show the same trend. Ph I, the 2nd pulse in the INTEGRAL band, accounts for ∼5% at 1 keV decreasing to ∼3% at 8 keV. Finally, Ph II is about constant in this energy range at a level of ∼2.5%. These trends are also visible in the phase-resolved pulsed spectra in Fig. 6.9, showing that at higher energies around 8 keV Ph III is dominating over the

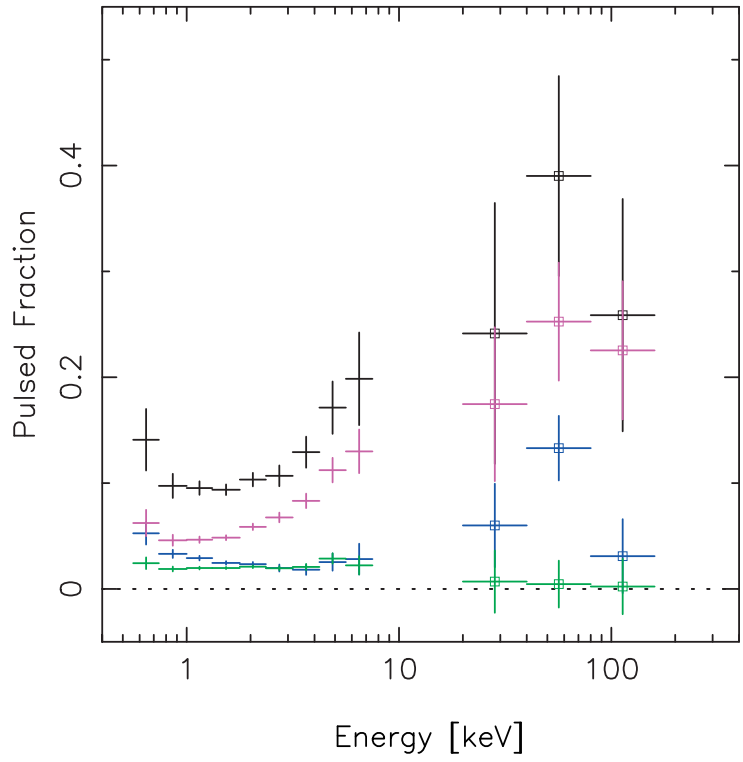

Figure 6.10: *Pulsed fraction as function of energy. Below 10 keV the averaged XMM-Newton pulsed fraction of observations A, B and C are plotted. Above 10 keV the INTEGRAL pulsed fraction is plotted. Consistent colour coding as Fig 6.8 and Fig. 6.9; Total-pulsed emission (black), Ph I (blue), Ph II (green), Ph III (magenta).*

other two phase intervals.

To investigate this further, the distribution of η is even more illustrative, as can be seen in Fig. 6.9 and Fig. 6.11: the contribution of Ph III to the total pulsed emission is steadily increasing with energy, reaching a fraction of $\sim$65% at 8 keV. For the avarage of the above reported RXTE-PCA observations (Fig. 6.8 the contribution from Ph III increases even to $\sim$100% around 10 keV. In the INTEGRAL band this contribution is again down to $\sim$60%–70%, due to the new pulse in Ph I.

In Fig. 6.9 is also clearly visible that during the ASCA-GIS observation the η of Ph III below 2 keV is less than that of Ph I. In all observations the η of Ph I is decreasing with energy from $\sim$30%–40% down to $\lesssim$5% around 8 keV. However, above 10 keV the contribution of Ph I is increasing again due to the 2nd pulse in the INTEGRAL band. Ph II, which was chosen as the DC level of unpulsed emission in the INTEGRAL band, shows first a constant η of $\sim$20% and

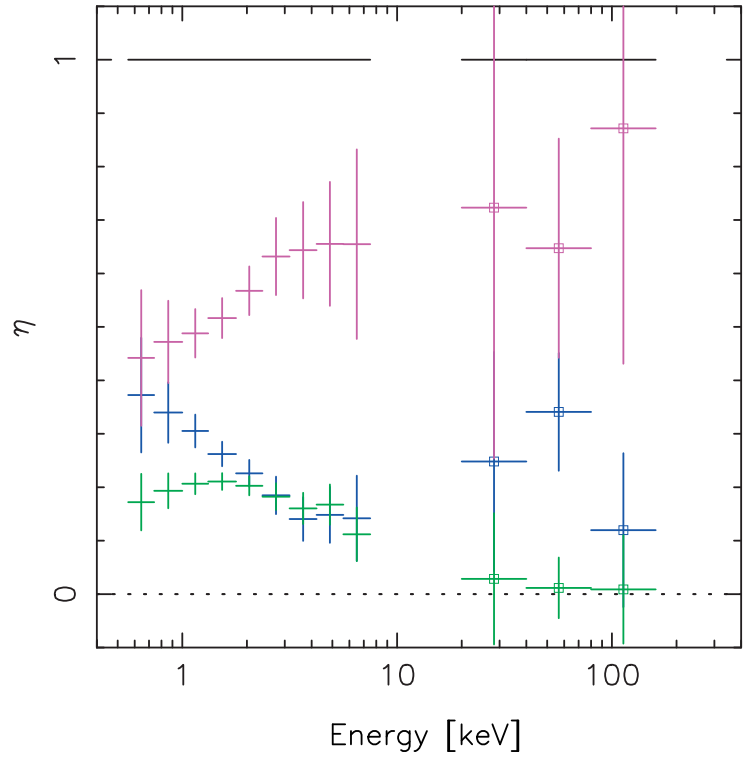

Figure 6.11: *Contribution to the total-pulsed emission* η *of the three selected phase intervals from the averaged XMM-Newton* η *of observations A, B and C and for INTEGRAL (>10 keV). Colour coding consistent with Fig. 6.10.*

it starts decreasing from 2 keV gradually to 0% in the INTEGRAL band.

6.4 Summary

In this paper we have presented new and more detailed characteristics of 4U 0142+61 in the hard X-ray regime (>10 keV) and studied these in a broader high-energy view using archival soft X-ray data (<10 keV) in consistent analyses. Many new or more accurate results are reported which should be considered in theoretical modelling of the high-energy emission from AXPs. Particularly new for studies of AXPs is the performed phase resolved spectroscopy over the total high-energy band, revealing distinctly different components contributing to the total emission. We will first present a summary of the results.

6.4.1 Total high-energy emission of 4U 0142+61

1) ISGRI measures with an effective exposure of 2.4 Ms the most accurate time-averaged total spectrum between 20 and 230 keV which is fully consistent with a power-law shape with index 0.93 ± 0.06 (*Sect. 6.3.1.2, Fig. 6.3 and Table 6.4*).
2) Combining ISGRI and SPI spectral data provides the first evidence at the $\sim 4\sigma$ level for a spectral break with maximum luminosity at an energy of $\sim$270 keV, assuming a logparabolic shape of the hard X-ray spectrum (*Sect. 6.3.1.2 and Fig. 6.3*).
3) The total high-energy spectrum, combining spectra measured with XMM-*Newton* and ISGRI, can be described satisfactorily with the sum of three logparabolic functions, two dominating the spectrum for energies below 8 keV and one above 20 keV (see also Rea et al. 2007c). Minimum values for the luminosity are reached around 10 keV (*Sect. 6.3.1.4, Fig. 6.3 and Table 6.5*).

6.4.2 Long-term variability in the total emission of 4U 0142+61

1) ISGRI does not see evidence for significant long-term variability of the source flux and power-law spectral index on one-year time scales between December 2003 and August 2006 at the 17% (1σ) level (*Sect. 6.3.1.1, Fig. 6.1 & 6.2 and Table 6.4*).
2) Two short INTEGRAL ToO observations following bursting behaviours of 4U 0142+61 measured with RXTE show the AXP to be in a state consistent with the time averaged flux and spectral shape. The total flux was stable within $\sim$20% (1σ; *Sect. 6.3.1.3*).

6.4.3 Pulse profiles

1) ISGRI measures above 20 keV significant hard-X-ray pulse profiles up to 160 keV (*Sect. 6.3.2.1 and Fig. 6.4*).
2) The morphologies of the profiles measured below 10 keV with XMM-*Newton* and ASCA-GIS differ from the hard-X-ray profile; one of the two X-ray pulses vanishes around 10 keV (confirmed with RXTE-PCA) and a new pulse appears above 20 keV (*Sect. 6.3.2.3 and Fig. 6.7*).
3) Three XMM-*Newton* observations in 2003–2004 give statistically identical pulse profiles, but the profile measured by ASCA-GIS in 1999 following a possible glitch of 4U 0142+61 (see also Morii et al. 2005b; Dib et al. 2007a) is significantly different with different relative strengths and spectra (0.8–10 keV) of the two pulses visible in the pulse profiles below 10 keV (*Sect. 6.3.2.2 and Fig. 6.5 & 6.6*).

6.4.4 Pulsed spectra

1) ISGRI measures above 20 keV a total-pulsed spectrum up to 160 keV with a shape consistent with a power law with index 0.40 ± 0.15, significantly different from that of the total spectrum. This implies that the difference spectrum, the DC component, is a genuinely different component (*Sect. 6.3.3.1, Fig. 6.8 and Table 6.7*).

2) Below 10 keV, there is evidence for long-term time variability. The total pulsed fluxes measured for the 0.8–2.0 keV band with ASCA-GIS in 1999 and in the three XMM-*Newton* observations in 2003–2004 are comparable, but in the 2.0–10.0 keV band different flux values are measured. The ASCA-GIS value is significantly lower by ∼35% than the mutually consistent XMM-*Newton* values, and the RXTE-PCA flux appears to be in between. The ∼35% decrease in total pulsed flux in the ASCA-GIS observation can largely be assigned to a decrease in the strength of only one of the X-ray pulses (*Sect. 6.3.3, Fig. 6.9 and Tables 6.7 & 6.8*). See also Dib et al. (2007a) for a significant increased pulsed flux of ∼36% since 2004 and during the bursting activities in 2006–2007 (Gonzalez et al. 2008).
3) The total pulsed fraction increases from ∼10% at 1 keV to possibly as high as ∼40% in the 40–80 keV band. Above these energies this fraction is uncertain, but might become close to 100%, depending on the actual shapes of the total and pulsed spectra (*Sect. 6.3.3.3 and Fig. 6.10*).

6.4.5 Phase-resolved pulsed spectra

1) Phase-resolved spectroscopy over the total high-energy band reveals the identification of at least three genuinely different pulse components with different spectra: a) a component in phase interval Ph III (phase 0.85–1.35) peaking at phase 1.1, present and dominant from 0.8 keV up to 160 keV. b) a hard-X-ray component in phase interval Ph I peaking in the ISGRI band above 20 keV at phase ∼0.55. c) a soft X-ray component in phase interval Ph I + Ph II (phase 0.35–0.85) peaking in the profiles for energies below 10 keV at phase ∼0.65, and not visible above 10 keV. d) the soft X-ray component mentioned in c), appears to consist of two parts, a softer contribution from phase interval Ph II than from phase interval Ph I, consistently seen for all reported X-ray observations (*Sect. 6.3.3, Fig. 6.9 and Tables 6.7 & 6.8*).
2) The total pulsed spectra and that of Ph III measured with RXTE (1996–2003) and consecutively with ISGRI (2003–2007) connect smoothly, and the phase-resolved spectra measured with ASCA (1999), XMM-*Newton* (2003–2004) and RXTE (1996–2003) are relatively similar. This is indicative of a remarkably stable geometry of the contributing emission sites at the surface and/or in the magnetosphere of the magnetar. There is no evidence for a drastic reordering (*Sect. 6.3.3.1, Fig. 6.8 and Table 6.7*).

6.5 Discussion

In this section, we discuss how these new findings fit within the theoretical models attempting to explain hard X-ray emission from AXPs. Before the discovery by INTEGRAL of non-thermal emission from AXPs above 10 keV, Cheng & Zhang (2001) modeled the production of high-energy gamma radiation in vacuum gaps proposed to be present in the outer magnetospheres of AXPs. Gamma-ray emission at the polar caps will be quenched due to the strong field, but far away from the pulsar surface gamma radiation could be emitted because the local field will drop below the critical quantum limit. This radio-pulsar scenario could offer a stable

configuration, suggested by our results to be required, but their model calculations do not reproduce the hard spectra and high X-ray luminosities found for e.g. 4U 0142+61. After the discovery by INTEGRAL three approaches were elaborated specifically to address the non-thermal, very luminous hard X-ray emission from AXPs: 1) a quantum electrodynamics model by Heyl & Hernquist (2005a,b); 2) a corona model by Beloborodov & Thompson (2007) and most recently by Lyubarsky & Eichler (2008); 3) a resonant upscattering model by Baring & Harding (2007). Below, we will consider each of these attempts.

6.5.1 Quantum electrodynamics model

Heyl & Hernquist (2005a) created a model to explain the origin of the SGR and AXP bursts through fast Quantum Electrodynamics (QED) wave modes which could be triggered when a starquake or other rearrangement in the magnetic field occurs. In their *fast-mode break down* model, magnetohydrodynamic (MHD) waves generated near the magnetar surface propagating outwards through the magnetosphere are altered by vacuum polarization. Hydrodynamic shocks can be developed and electron-positron pairs produced. An optically thick fireball could be created emitting mainly X and gamma rays, which can be observed as a SGR or an AXP burst. To explain stable non-thermal emission Heyl & Hernquist (2005b) extended this model to weaker fast modes that do not create an optically thick fireball. The resulting spectrum depends on the total energy delivered by the fast mode and the maximum magnetic field strength. The latter value determines two energy values where the spectrum breaks. The peak energy in the spectrum is given by $E_{\rm break} \approx 1600 \frac{B_{\rm crit}}{B} mc^2$, where $B_{\rm crit}$ is the quantum critical field of 4.4×10^{13} G, and B the neutron-star magnetic field. The other break energy is given by $E_0 \approx 10^{-6} \frac{B}{B_{\rm crit}} mc^2$. The spectral shapes below, between and above these break energies are power-law like with photon indices of 0, 1.5 and 3, respectively. The power law below E_0 can extend down to the optical regime, in which pulsed non-thermal optical emission (Eichler et al. 2002) has been detected from 4U 0142+61 (Hulleman et al. 2004; Kern & Martin 2002; Dhillon et al. 2005).

Peak energies predicted by this model all exceed 1 MeV. The fast mode cascade of pairs is not effective if the energy in the pairs ($E_{\rm break}$) is less than $2mc^2$. This natural limit is called the *minimal model* where $E_{\rm break} \approx 1$ MeV. In this case, the pairs are created in a (local) magnetic field much weaker than $B_{\rm crit}$. Heyl (2007) examined the angular dependence of the non-thermal emission in the weak field regime ($B_{\rm NS} \ll B_{\rm crit}$). The produced spectrum strongly depends on the angle between the magnetic field and the wave propagation direction. Specifically, the non-thermal hard X-ray emission is expected to be largest when the observer's viewing direction to the pulsar is perpendicular to the local magnetic field, while the thermal emission is expected to peak when the observer views the polar regions. The difference between the phases at which the thermal and non-thermal emissions are peaking can range between 90° and 180° if the angles $\alpha + \beta \geq 90°$, where α is the angle between the rotation axis and the observer's line of sight and β the angle between the rotation axis and the magnetic (dipole) axis. If $\alpha + \beta < 90°$, then the phase difference between the non-thermal and the

thermal emission is 180°.

Comparing the above QED model predictions with our results, we note that the power-law spectral index of the total emission above 20 keV of 4U 0142+61, 0.93±0.06, is harder than the predicted value of 1.5. Furthermore, the estimated break energy of ∼270 keV is far below the allowed minimum value of ∼1 MeV, and would mean a neutron star magnetic field strength of 1.3×10^{16} G. The spectral index of the total pulsed emission of 0.40±0.15 is inconsistent with the value 1.5. We note that Heyl & Hernquist (2005a) do not make a distinction between the pulsed and total emission.

Finally, there is a clear prediction of a phase difference between the thermal and non-thermal emission: Our phase-resolved spectroscopy shows that the actual situation is much more complex: one pulse exhibits a spectrum composed of a thermal *and* a non-thermal component in the same phase interval (Ph III); the thermal pulse in phase interval Ph I+II seems to vanish above 10 keV and a non-thermal pulse shows up above 20 keV in Ph II, also at a negligible phase difference.

6.5.2 Corona model

The corona model developed by Beloborodov & Thompson (2007) is an extension of earlier work by Thompson & Beloborodov (2005) and Thompson et al. (2002). Thompson et al. (2002) extended the magnetar model by a twisted magnetosphere, which was introduced by Thompson et al. (2000) to explain some observational characteristics seen in SGR 1900+14. Accordingly, the assumed dipolar field gets twisted due to continuous seismic activity as a result of the extreme internal magnetic field and a quasi stable loop (tube) can be formed with a maximum radius of ∼2 R_{NS}.

Essential in this scenario is an electric field parallel to the magnetic field which is generated by self induction. This parallel electric field is capable of accelerating particles and initiates an electron-positron avalanche. In this way, toroidal field (magnetic) energy is converted into particle kinetic energy. The energy production in the tube is related to the voltage difference (Φ_e) between the footpoints of the loop. The dissipation rate is given by $L_{\rm diss} \sim 10^{37} \Delta\phi (B/10^{15}{\rm G})(a/R_{\rm NS})(e\Phi_e/{\rm GeV})$ erg s^{-1}, where $\Delta\phi$ is the twist angle (in radians) and a is the size of the twisted region. $e\Phi_e$ must be sufficiently high for charged particles to be lifted from the surface of the neutron star (∼200 MeV) or to create pairs in the magnetosphere ($\sim\gamma_\pm mc^2 = 0.5\gamma_\pm$ MeV) which are accelerated to ∼0.1–1 GeV.

If the voltage is too low to create a plasma, the tube regulates itself by either reducing the current or an electric field is generated ($\partial\mathbf{E}/\partial t \sim \nabla\times$ **B** – **j**) until it is high enough to provide the plasma. If the voltage is too high, the parallel electric field will be screened by polarization of the plasma. Through this self-regulating voltage 'constant' pair production is achieved, feeding the high-energy emission. The dissipation time scale of the loop, i.e. the unwinding of the twist, is of the order 1–10 years. It is determined by the voltage difference Φ_e and the corona luminosity $L_{\rm diss}$. For a global twist of a dipole this becomes: $t_{\rm decay} = 0.8(R_{\rm NS}/c^2)L_{\rm diss}/{\Phi_e}^2$. Therefore, the stronger a twist (brighter corona) the longer the live time.

The downward beam of electrons and positrons through the tube will heat a transition layer between the atmosphere and the corona up to ∼200 keV, radiating bremsstrahlung to cool. In this thermal transition layer additional pairs can be created after electron ion collisions. The emerging spectrum will have a power-law shape with index $\Gamma \sim 1$ below the break energy. These bremsstrahlung photons can convert into pairs if the photon energy exceeds $2m_e c^2 / \sin\theta$. In that case synchrotron emission will be produced. Either way, the maximum energy of photons escaping the strong magnetic field is ∼1 MeV.

Beloborodov & Thompson (2007) also address the production of non-thermal emission below the INTEGRAL-ISGRI energy window. In the 2–10 keV band resonant upscattering of keV photons can explain the soft power-law like X-ray tail (>5 keV) to the black-body component as first described by Thompson et al. (2002) (see also Lyutikov & Gavriil 2006; Güver et al. 2006; Fernández & Thompson 2007). For the non-thermal optical and NIR emission four possible emission mechanisms are discussed with a curvature-radiation origin being the most plausible explanation. See also the interpretation of the NIR, optical and soft X-ray observations by Hulleman et al. (2004), Morii et al. (2005a) and Durant & van Kerkwijk (2006c).

A critical aspect in the corona model is the dissipation time scale of the twist. This determines how long a quasi stable loop can produce a non-thermal component in the pulse profile. Once the loop vanishes, the pulse profile should drastically change shape. When a next starquake produces a new tube, a new non-thermal pulse at a different phase should appear in the profile. The unwinding of such quasi stable loops feeds the non-thermal emission, and it seems plausible that also long-term flux variability occurs. Our results give increasing evidence that the non-thermal emission and the global structure of the pulse profile are stable over many years. During the INTEGRAL observations covering more than three years, we do not see significant variation in intensity and spectral shape of the total and pulsed emission above 20 keV. Furthermore, the RXTE monitoring observations covering the eight years before the INTEGRAL observations give time-averaged spectra for the total and total pulsed emission, as well as for the spectrum of the main pulse (Ph III) in the pulse profile that connect smoothly to the INTEGRAL-ISGRI spectra. In addition, the pulse maxima and the minima in the pulse profiles measured by ISGRI and RXTE line-up, suggesting a very stable geometry and intensity at hard X-rays over more than 10 years. This seems to be at the limit of what the corona model still can sustain for a bright corona.

The proposed bremsstrahlung spectrum with index $\Gamma \sim 1$ (Beloborodov & Thompson 2007) is consistent with our total spectrum for 4U 0142+61 with $\Gamma = 0.93 \pm 0.06$ below the break energy. However, we showed that the total pulsed spectrum is much harder with $\Gamma = 0.40 \pm 0.15$, and, as a consequence, the DC difference spectrum much softer, both not consistent with a bremsstrahlung origin. The DC spectrum extends at least up to 100 keV, given the pulsed fraction of $\sim 50\%$ at these high energies.

Lyubarsky & Eichler (2008) revisited the heating by the downward beam of electrons and positrons of the transition region and conclude that this mechanism is incapable of heating the atmosphere due to suppression of the required two-stream instability. They propose, rather, that a hot, tenuous atmosphere forms with a temperature of ∼1–2 MeV, an order of magni-

tude larger than inferred by Thompson & Beloborodov (2005) and Beloborodov & Thompson (2007). In this hot atmosphere hard radiation is generated via bremsstrahlung. Furthermore, pairs are easily produced and fill the whole magnetosphere forming a hot corona. In the latter collisionless interaction of the primary beam with the pair plasma in the corona heats the pairs even more. Most of this coronal energy is released in the hard X-ray and soft gamma-ray bands by Comptonization, so that the overall spectrum of the source is a superposition of bremsstrahlung radiation from the hot atmosphere and Comptonization radiation from the extended corona. The latter radiates in all directions, and the spectrum extends to the MeV band. The Comptonization radiation dominates below $\sim$100 keV with photon spectral slope of $\Gamma \sim$1–2, with a bremsstrahlung spectrum ($\Gamma \sim 1$) above this break energy. This overall spectral shape is not consistent with our results on 4U 0142+61. The Comptonization spectral shape below the break energy might be marginally consistent with that of the total spectrum, but by far too soft for the total pulsed spectrum. Furthermore, a bremsstrahlung spectrum after the break energy would mean an upturn of the spectrum, extending up to the MeV band. This is inconsistent with the INTEGRAL-SPI results above 100 keV and more importantly, with the COMPTEL upper limits in the MeV band. Finally, it is hard to imagine how a Comptonization component originating in an extended corona radiating in all directions can produce the phase distribution of 4U 0142+61 with well defined pulses and, for 4U 0142+61, a sharp minimum.

Our concerns on the long-term stability/variability of the corona model as expressed for the work by Beloborodov & Thompson (2007), are also valid for the approach of Lyubarsky & Eichler (2008).

6.5.3 Compton upscattering model

Baring & Harding (2007) consider resonant, magnetic Compton upscattering to explain the hard X-ray emission. Ultra-relativistic electrons, accelerated along either open or closed magnetic field lines, upscatter the thermal soft X-ray atmospheric photons. This process is very effective close to the magnetar surface ($\lesssim 10 R_{\rm NS}$) where the magnetic field is still strong. For high-B isolated pulsars it is shown that acceleration of electrons to ultra-relativistic energies can occur (e.g. Sturner 1995; Harding & Muslimov 1998; Dyks & Rudak 2000). However, if AXPs with their long periods have also a dipolar structure at the surface, the acceleration zone cap radii would become extremely small (of order 50 m). As a result, the relativistic electrons would have to be concentrated in such a narrow column with charge densities far exceeding the Goldreich-Julian maximum density (Goldreich & Julian 1969). They argue, however, that non-dipolar structure at the surface is energetically feasible, allowing the electron acceleration zone to cover a much larger range of colatitudes than assigned to a standard polar cap.

The Compton scattering formalism invokes full relativistic and relativistic QED effects in high magnetic fields. Referring to earlier studies by i.e. Daugherty & Harding (1986); Ho & Epstein (1989) and Gonthier et al. (2000), and applications in the magnetic Thomson limit for old gamma-ray burst scenarios (Dermer 1990; Baring 1994) and for pulsar contexts (Daugherty & Harding 1989; Sturner et al. 1995), Baring & Harding (2007) make a first attempt to

calculate geometries and emission spectra produced in the 'resonasphere' of AXPs for a simplified scenario. They consider the case for a magnetic dipole field geometry and an injected monoenergetic electron distribution as well as monoenergetic incident photons of energy commensurate with the thermal photon temperatures $kT \sim 0.5 - 1$ keV observed in AXPs. Important first conclusions are that the Compton resonasphere for long period AXPs is confined to within few stellar radii of the surface at higher field locales, and that the emission spectra are considerably softer than the hard X-ray tails seen in AXPs, and extend to energies higher than allowed by the COMPTEL upper limits, as e.g. shown in Fig. 6.3. The spectra do break above a maximum photon energy which is dependent on the magnetic field and the Lorentz factor. Furthermore, the observed spectra depend very sensitively on the viewing direction of the observer with respect to the magnetospheric geometry. For investigating such predictions, phase-resolved spectroscopy as applied in this work offers a very sensitive diagnostic tool. However, more complicated modelling addressing non-dipolar field topologies and more realistic electron and photon spectra are required before our detailed findings can be confronted with the predictions for hard X-ray emission from resonant Compton upscattering in AXPs. What can be noted, is that the preliminary example spectra derived by Baring & Harding (2007) are too soft and extend to energies much higher than can be permitted by the COMPTEL upper limits.

6.5.4 Concluding remark

The above discussions indicate that our detailed results as summarized in the previous section require, for all attempts to model the non-thermal emission above 20 keV, consideration of a full three-dimensional geometry taking the relevant angles (magnetic axis with respect to spin axis, viewing angle) into account, as well as the physical production processes taking place on the surface of the neutron star and in different sites of the atmosphere and magnetosphere. Such analysis would be similar to what is done to model the non-thermal emission from radio pulsars. Our results seem to indicate that the non-thermal persistent emission from AXPs is persistent, requiring a scenario with a stable geometry. To obtain further information on the geometry, including more information for the different relevant angles, similar detailed results for the other non-thermally emitting AXPs (see Kuiper et al. 2006) are important to give further constraints on the theoretical modelling.

Acknowledgements. We would like to acknowledge: C. Winkler, INTEGRAL Project Scientist and the INTEGRAL team for the quick ToO response; F. Haberl for useful discussions on how to analyse the XMM-Newton timing data correctly. This work is supported by NWO, Netherlands Organisation for Scientific Research. RD is supported by the Natural Sciences and Engineering Research Council (NSERC) PGSD scholarship. FPG is supported by the NASA Postdoctoral Program administered by Oak Ridge Associated Universities at NASA Goddard Space-Flight Center. Additional support was provided by NSERC Discovery Grant Rgpin 228738-03, FQRNT, CIFAR, and CFI. VMK holds a Lorne Trottier Chair in Astrophysics & Cosmology, a Canada Research Chair and is a R. Howard Webster Foundation Fellow of CIFAR. The results are based on observations with INTEGRAL, an ESA project with instruments

and science data centre funded by ESA member states (especially the PI countries: Denmark, France, Germany, Italy, Switzerland, Spain), Czech Republic and Poland, and with the participation of Russia and the USA. The SPI project has been completed under the responsibility and leadership of CNES. We are grateful to ASI, CEA, CNES, DLR, ESA, INTA, NASA and OSTC for support. This research has made use of data obtained through the High-Energy Astrophysics Center Online Service, provided by the NASA/Goddard Space-Flight Center.